

Eikonal minijet model for proton–proton collisions

Master's thesis, March 31, 2017

Author:

MIKKO KUHA

Supervisor:

KARI J. ESKOLA



UNIVERSITY OF JYVÄSKYLÄ

Abstract

An eikonal minijet model for high energy proton–proton collisions was discussed and numerically tested. The testing was done against data gathered on elastic, inelastic, and total cross-sections in proton–proton collisions at the centre of momentum frame energy scale of $\sqrt{s} = 0.1 \dots 100$ TeV, including the latest CERN–LHC measurements. As a part of the numerical analysis, the validity of the single effective subprocess approximation was examined, and the contributions of multiple dijet production to the inelastic cross-section were calculated separately. The analytically simplistic eikonal minijet model performed surprisingly well in the data comparison when the width of the gluon cloud was chosen large enough. Also, the single effective subprocess approximation was demonstrated to work to a very good accuracy at the energy scales studied.

Tiivistelmä

Tässä tutkielmassa johdettiin minijettimalli suurienergisille protoni–protoni -törmäyksille eikonaaliformalismissa. Mallia testattiin numeerisen laskennan keinoin kokeellisilla tuloksilla protoni–protoni -törmäyksiä elastisista, epäelastisista ja kokonaisvaikutusaloista keskeisliikemääräkoordinaatiston energiaskaalassa $\sqrt{s} = 0.1 \dots 100$ TeV. Myös viimeisimpiä CERN–LHC -kiihdyttimen mittaus-tuloksia tarkasteltiin. Numeerisen analyysin yhtenä osana tutkittiin myös yhden efektiivisen aliprosessin approksimaatiota, joka osoittautui tutkituilla energioilla hyvin tarkaksi. Lisäksi tarkasteltiin moninkertaisen kaksijettituoton roolia protoni–protoni -törmäysten epäelastisessa vaikutusalueella.

Contents

1	Introduction	1
2	Dijet production in proton–proton collisions	3
2.1	Subprocesses	6
2.2	Integrated dijet production cross-section	10
3	Eikonal approximation	15
3.1	Solving Schrödinger equation	15
3.2	Solving scattering amplitude	18
3.3	Scattering cross-sections	21
4	Eikonal minijet model	25
5	Numerical calculations	29
5.1	Calculating cross-sections	29
5.2	Fitting transverse momentum cutoff	30
5.3	Contributions of multiple minijet production	31
5.4	Conservation of momentum?	31
6	Results	33
7	Conclusion	43
A	Quantum Chromodynamics tools	51
A.1	Gluon propagators	51
A.2	Polarisation tensor in Lorenz gauge	55

A.3	Polarisation tensor in axial gauge	58
B	Integrating in momentum fraction space	61

Chapter 1

Introduction

In our quest to understand the building blocks of the universe we live in, we have developed the Standard Model of particle physics. It is the summit of our current knowledge about the fundamental particles and the ways they interact with each other. Within the Standard Model, the strong nuclear force is nowadays thought to be best described by Quantum Chromodynamics (QCD).

Not only are the nuclei of the atoms, but also the very constituents of those nuclei, protons and neutrons, held together by QCD interactions. Rather than being indivisible elementary particles, protons and neutrons, and other hadrons are actually ensembles of quarks, antiquarks, and gluons, collectively called partons. These partons we can unfortunately not study directly, as they eventually may only appear in colour neutral hadron states. This phenomenon is called colour confinement.

The way to study the properties and interactions of partons is through indirect measurements. We collide hadrons onto each other with such high energies that their inner structure breaks, and then observe the results. The produced multitudes of new particles tell us about the mentioned inner structure of the hadrons and thus also about QCD.

In this thesis, the background for an eikonal minijet model for proton–proton collisions will be presented, and its applicability will be studied via numerical analysis and comparison with experimental data. The vital parts for the model arising from perturbative QCD and parton model will be shown in Chapter 2. Chapter 3 focuses on a quantum scattering problem: the eikonal formalism will be derived in analogue with the classical scattering problem of lightwaves. After the theoretical foundation is laid, the eikonal minijet model is presented in Chapter 4. This marks the turning point of the thesis, as in Chapter 5 the focus will be turned

to the methods of numerical analysis. Chapter 6 will then continue along these lines, and the results of the numerical analysis will be presented. Some concluding remarks will be discussed in Chapter 7.

The majority of the work behind this thesis was in the numerical analysis. The author continued from his symbolical perturbative QCD (pQCD) calculations in his research training in summer 2016 to build from scratch the program used in the numerical analysis. Most of the work was thus done during autumn 2016.

Chapter 2

Dijet production in proton–proton collisions

In this chapter, we will introduce the jet-production formalism in proton–proton collisions in the leading order ($\mathcal{O}(\alpha_s^2)$, α_s is the QCD coupling constant) of perturbative QCD. The basic process of interest here is an ultrarelativistic inclusive inelastic scattering $p+p \rightarrow \text{jet}+\text{jet}+X$, where X can be anything. The discussion will follow those in my research thesis report [1] and in the lecture notes of the course FYSH556 perturbative QCD [2].

According to the parton model [3, 4], protons and other hadrons are thought to be collections of collinearly, longitudinally, moving quarks, antiquarks, and gluons, collectively named partons. A proton–proton collision, therefore, is an event of colliding partons. To the leading order in pQCD, if the interaction scale (transverse momentum exchange) is large enough so that $\alpha_s \ll 1$, two onshell partons can scatter from each other only in $2 \rightarrow 2$ processes. Due to the colour confinement, partons must, in the very end of the collision, end up in colour neutral hadron states. This causes the event products, partons of large transverse momenta, to hadronize into well-collimated showers of hadrons called jets. The problem in question, therefore, consists of two clearly discrete levels: dijet production in proton–proton collision on the hadron level, and $2 \rightarrow 2$ scattering process on the parton level. On an interesting sidenote, as the parton level calculations are independent of the hadron level particles, these can be applied to any hadron–hadron, or even hadron–nucleus or nucleus–nucleus collisions.

Figure 2.1 illustrates the situation in the parton model for the process $p + p \rightarrow \text{jet} + \text{jet} + X$. The initial state partons labelled i and j interact via the strong interaction. Let us label the end products of the partonic $2 \rightarrow 2$ scattering process as partons k and l . We assume that the energy scale of the process, the transverse

momentum of the partons, is of such a high magnitude that due to the running of the strong coupling constant α_s the process can be approximated with the leading order QCD perturbation theory.

Consider the centre of momentum frame of the colliding protons so that the protons have equal but opposite four-momenta h_1 and h_2 . Then the partons i and j have longitudinal momenta $x_1 h_1$ and $x_2 h_2$, respectively, where $x_1, x_2 \in [0, 1]$ are the momentum fractions of the partons. In the transverse direction, the momenta of the initial state partons can be assumed to be negligible. Let us name the momenta of the event product partons k and l as k_1 and k_2 , respectively. These momenta have longitudinal components k_{1L} and k_{2L} , and transverse momentum vectors \mathbf{k}_{1T} and \mathbf{k}_{2T} orthogonal to the momenta of the protons. Label also the energies of the partons k and l with symbols E_1 and E_2 , respectively. As shown below, due to momentum conservation, the transverse vectors must be equal but opposite, i.e. $\mathbf{k}_{1T} = -\mathbf{k}_{2T}$. Therefore we can label the transverse momentum with $k_T = |\mathbf{k}_{1T}| = |\mathbf{k}_{2T}|$. The rapidity y_1 of the parton k is defined as

$$y_1 = \frac{1}{2} \log \frac{E_1 + k_{1L}}{E_1 - k_{1L}}. \quad (2.1)$$

The rapidity y_2 of the particle l is defined similarly.

With these definitions now the parton level subprocess cross-section can then be written as [2] [5, ch. 4.5]

$$d\hat{\sigma}^{i+j \rightarrow k+l} = \frac{1}{2\hat{s}} \frac{d^3 k_1}{(2\pi)^3 2E_1} \frac{d^3 k_2}{(2\pi)^3 2E_2} \langle |\mathcal{M}_{i+j \rightarrow k+l}|^2 \rangle (2\pi)^4 \delta^{(4)}(x_1 h_1 + x_2 h_2 - k_1 - k_2) \quad (2.2)$$

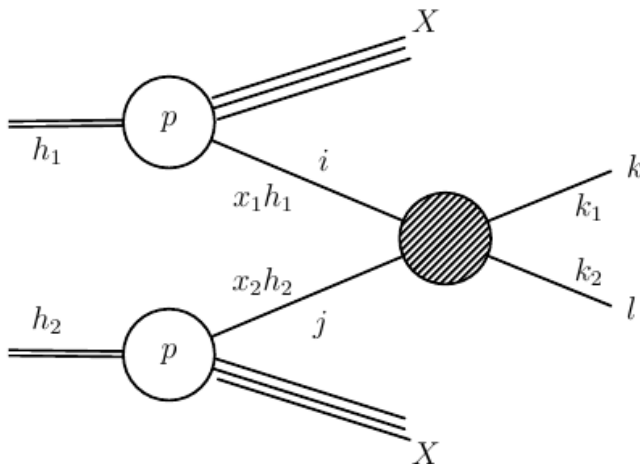


Figure 2.1: Dijet production in proton–proton collision in the parton model. Symbols i and j label the initial state partons from the colliding protons p , and k and l are the partons that eventually hadronize to form the outgoing jets. Also the four-momenta as explained in the text are shown.

where the parton level Mandelstam variable $\hat{s} = (x_1 h_1 + x_2 h_2)^2$, $\frac{d^3 k_{1,2}}{(2\pi)^3 2E_{1,2}}$ are the Lorentz invariant integral measures, $\langle |\mathcal{M}|^2 \rangle$ is the Lorentz invariant squared scattering amplitude averaged over spin/polarisation and colour states, and $\delta^{(4)}$ is the Dirac delta distribution in four dimensions. Now using [5, 6]

$$\frac{d\hat{\sigma}}{d\hat{t}} = \frac{\langle |\mathcal{M}|^2 \rangle}{16\pi\hat{s}^2} \quad (2.3)$$

and the collinear factorization theorem [7, ch. 14.3], the differential cross-section of the dijet production to leading order in perturbative QCD can be written as

$$\begin{aligned} & E_1 E_2 \frac{d\sigma^{p+p \rightarrow \text{jett}+\text{jett}+X}}{d^3 k_1 d^3 k_2} \\ &= \sum_{i,j,k,l} \int_0^1 dx_1 dx_2 f_i(x_1, Q^2) f_j(x_2, Q^2) \cdot \frac{\hat{s}}{2\pi} \frac{d\hat{\sigma}^{i+j \rightarrow k+l}}{d\hat{t}} \delta^{(4)}(x_1 h_1 + x_2 h_2 - k_1 - k_2), \end{aligned} \quad (2.4)$$

where $Q^2 \approx k_T^2$ is the interaction energy scale and the parton level Mandelstam variable $\hat{t} = (x_1 h_1 - k_1)^2$. The functions f_i and f_j are the parton distribution functions (PDFs) of partons i and j . These distributions cannot be predicted from perturbative QCD, but they must be measured experimentally as they are inherently nonperturbative objects. The PDFs are, however, process-independent, so that results of experiments on other processes (e.g. deep inelastic scattering, Drell-Yan dilepton production) can be combined. Even though the PDFs cannot be derived from pQCD, their scale evolution is governed by the DGLAP Equations [8, 9, 10, 11] of pQCD. The summation over i, j, k, l in Equation (2.4) will be discussed in more detail in Section 2.2.

Using the well-known identities of the Dirac delta distribution, one can easily show that

$$\begin{aligned} & \delta^{(4)}(x_1 h_1 + x_2 h_2 - k_1 - k_2) \\ &= \frac{2}{s} \delta^{(2)}(\mathbf{k}_{1T} + \mathbf{k}_{2T}) \delta\left(x_1 - \frac{k_T}{\sqrt{s}} (e^{y_1} + e^{y_2})\right) \delta\left(x_2 - \frac{k_T}{\sqrt{s}} (e^{-y_1} + e^{-y_2})\right), \end{aligned} \quad (2.5)$$

where the hadron level Mandelstam variable $s = (h_1 + h_2)^2$. Inserting (2.5) into (2.4) and integrating over \mathbf{k}_{2T} yields the differential cross-section

$$\frac{d\sigma^{p+p \rightarrow \text{jett}+\text{jett}+X}}{dk_T^2 dy_1 dy_2} = \sum_{i,j,k,l} x_1 f_i(x_1, Q^2) \cdot x_2 f_j(x_2, Q^2) \cdot \frac{d\hat{\sigma}^{i+j \rightarrow k+l}}{d\hat{t}}, \quad (2.6)$$

where the momentum fractions are

$$x_1 = \frac{k_T}{\sqrt{s}} (e^{y_1} + e^{y_2}), \quad (2.7)$$

$$x_2 = \frac{k_T}{\sqrt{s}} (e^{-y_1} + e^{-y_2}). \quad (2.8)$$

2.1 Subprocesses

The leading order in perturbative QCD allows for eight different types of $2 \rightarrow 2$ processes for quarks, antiquarks, and gluons. These processes are shown in Table 2.1. In this section, we will make a brief overview of how the cross-sections of those are calculated.

One can see multiple similarities between the processes in Table 2.1. In fact, many of the different Feynman diagrams can be calculated from each other by crossing external legs and changing the colour factor. The graph of process 3 can be obtained from that of the process 1, the graphs of the process 4 can be obtained from those of the process 2, and the graphs of the processes 6 and 7 from the graphs of the process 5. In the process 8, one can make use of a crossing between the t , u , and s - channels.

Using the Feynman rules in Appendix A, the squared, colour and spin/polarisation averaged invariant amplitudes of the processes 1–7 are straightforwardly calculated even by hand. These calculations can be found e.g. in [2]. The process 8, on the other hand, deserves some special attention.

The process $g + g \rightarrow g + g$ can happen via four topologically different channels in the leading order of QCD perturbation theory. These channels are represented in Figure 2.2. The invariant amplitudes of these channels are of the form

$$\mathcal{M}' = \mathcal{M}_{\mu_1\mu_2\mu_3\mu_4}^{a_1a_2a_3a_4}(p_1, p_2, p_3, p_4) \times \epsilon_{\lambda_1}^{\mu_1}(p_1) \times \epsilon_{\lambda_2}^{\mu_2}(p_2) \times \epsilon_{\lambda_3}^{*\mu_3}(p_3) \times \epsilon_{\lambda_4}^{*\mu_4}(p_4), \quad (2.9)$$

where the tensors ϵ are polarisation vectors. The tensors $\mathcal{M}_{\mu_1\mu_2\mu_3\mu_4}^{a_1a_2a_3a_4}$ have in the Feynman gauge the form

$$\begin{aligned} \mathcal{M}_{\mu_1\mu_2\mu_3\mu_4}^{a_1a_2a_3a_4} = & -g_s f^{a_3a_1c} \left(g_{\mu_3\mu_1}(-p_3 - p_1)_\mu + g_{\mu_1\mu}(2p_1 - p_3)_{\mu_3} + g_{\mu\mu_3}(-p_1 + 2p_3)_{\mu_1} \right) \\ & \times \left[-\frac{i\delta^{cd}g^{\mu\nu}}{(p_1 - p_3)^2} \right] \times \\ & (-g_s) f^{a_2a_4d} \left(g_{\mu_2\mu_4}(p_2 + p_4)_\nu + g_{\mu_4\nu}(-2p_4 + p_2)_{\mu_2} + g_{\nu\mu_2}(p_4 - 2p_2)_{\mu_4} \right), \end{aligned}$$

Table 2.1: Differential cross-sections of the partonic subprocesses in jet production at leading order (α_s^2) pQCD. [1, 12, 13]

Subprocess	Topologically different Feynman diagrams in LO pQCD	$\frac{\hat{s} d\hat{\sigma}}{\pi d\hat{t}} \cdot \frac{\hat{s}}{\alpha_s^2} = \frac{\langle \mathcal{M} ^2 \rangle}{16\pi^2 \alpha_s^2}$
1 $q_i + q_j \rightarrow q_i + q_j$ or $q_i + \bar{q}_j \rightarrow q_i + \bar{q}_j,$ $i \neq j$		$\frac{4}{9} \frac{\hat{s}^2 + \hat{u}^2}{\hat{t}^2}$
2 $q_i + q_i \rightarrow q_i + q_i$		$\frac{4}{9} \left(\frac{\hat{s}^2 + \hat{u}^2}{\hat{t}^2} + \frac{\hat{s}^2 + \hat{t}^2}{\hat{u}^2} - \frac{2\hat{s}^2}{3\hat{t}\hat{u}} \right)$
3 $q_i + \bar{q}_i \rightarrow q_j + \bar{q}_j,$ $i \neq j$		$\frac{4}{9} \frac{\hat{t}^2 + \hat{u}^2}{\hat{s}^2}$
4 $q_i + \bar{q}_i \rightarrow q_i + \bar{q}_i$		$\frac{4}{9} \left(\frac{\hat{s}^2 + \hat{u}^2}{\hat{t}^2} + \frac{\hat{t}^2 + \hat{u}^2}{\hat{s}^2} - \frac{2\hat{u}^2}{3\hat{s}\hat{t}} \right)$
5 $q_i + \bar{q}_i \rightarrow g + g$		$\frac{8}{3} (\hat{t}^2 + \hat{u}^2) \left(\frac{4}{9\hat{t}\hat{u}} - \frac{1}{\hat{s}^2} \right)$
6 $g + g \rightarrow q_i + \bar{q}_i$		$\frac{3}{8} (\hat{t}^2 + \hat{u}^2) \left(\frac{4}{9\hat{t}\hat{u}} - \frac{1}{\hat{s}^2} \right)$
7 $g + q_i \rightarrow g + q_i$		$(\hat{s}^2 + \hat{u}^2) \left(\frac{1}{\hat{t}^2} - \frac{4}{9\hat{s}\hat{u}} \right)$
8 $g + g \rightarrow g + g$		$\frac{9}{2} \left(3 - \frac{\hat{t}\hat{u}}{\hat{s}^2} - \frac{\hat{s}\hat{u}}{\hat{t}^2} - \frac{\hat{s}\hat{t}}{\hat{u}^2} \right)$

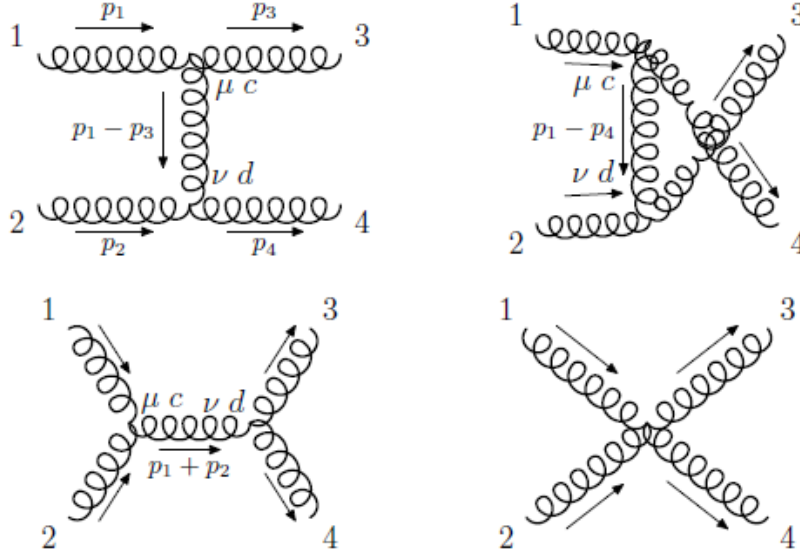


Figure 2.2: Feynman diagrams of the topologically different channels of the process $g + g \rightarrow g + g$ in the leading order of perturbative QCD. From the top left corner: channels t , u , s , and $4g$. The real gluons 1 and 2 are the initial particles in the process, and 3 and 4 are the products. The colours of these external legs are a_i and polarisations λ_i with $i = 1 \dots 4$. The arrows show the chosen momentum arrangement.

$$\begin{aligned} \mathcal{M}_u^{a_1 a_2 a_3 a_4} &= -g_s f^{a_4 a_1 c} \left(g_{\mu_4 \mu_1} (-p_4 - p_1)_\mu + g_{\mu_1 \mu} (2p_1 - p_4)_{\mu_4} + g_{\mu \mu_4} (-p_1 + 2p_4)_{\mu_1} \right) \\ &\quad \times \left[-\frac{i \delta^{cd} g^{\mu\nu}}{(p_1 - p_4)^2} \right] \times \\ &\quad (-g_s) f^{a_2 a_3 d} \left(g_{\mu_2 \mu_3} (p_2 + p_3)_\nu + g_{\mu_3 \nu} (-2p_3 + p_2)_{\mu_2} + g_{\nu \mu_2} (p_3 - 2p_2)_{\mu_3} \right), \end{aligned}$$

$$\begin{aligned} \mathcal{M}_s^{a_1 a_2 a_3 a_4} &= -g_s f^{a_1 a_2 c} \left(g_{\mu_1 \mu_2} (p_1 - p_2)_\mu + g_{\mu_2 \mu} (2p_2 + p_1)_{\mu_1} + g_{\mu \mu_1} (-p_2 - 2p_1)_{\mu_2} \right) \\ &\quad \times \left[-\frac{i \delta^{cd} g^{\mu\nu}}{(p_1 + p_2)^2} \right] \times \\ &\quad (-g_s) f^{a_4 a_3 d} \left(g_{\mu_4 \mu_3} (-p_4 + p_3)_\nu + g_{\mu_4 \nu} (-2p_3 - p_4)_{\mu_3} + g_{\nu \mu_3} (p_3 + 2p_4)_{\mu_4} \right), \end{aligned}$$

and

$$\begin{aligned} \mathcal{M}_{4g}^{a_1 a_2 a_3 a_4} &= -i g_s^2 \left[f^{ca_1 a_2} f^{ca_3 a_4} (g_{\mu_1 \mu_3} g_{\mu_2 \mu_4} - g_{\mu_1 \mu_4} g_{\mu_2 \mu_3}) \right. \\ &\quad + f^{ca_1 a_3} f^{ca_4 a_2} (g_{\mu_1 \mu_4} g_{\mu_3 \mu_2} - g_{\mu_1 \mu_2} g_{\mu_3 \mu_4}) \\ &\quad \left. + f^{ca_1 a_4} f^{ca_2 a_3} (g_{\mu_1 \mu_2} g_{\mu_4 \mu_3} - g_{\mu_1 \mu_3} g_{\mu_4 \mu_2}) \right], \end{aligned}$$

where g_s is the strong coupling constant ($\alpha_s^2 = \frac{g_s^2}{4\pi}$), f^{abc} are the structure constants of SU(3), $g^{\mu\nu}$ is the metric tensor and δ^{ab} is the Kronecker delta. The squared averaged invariant amplitude of the whole process then gets the form

$$\begin{aligned}
\langle |\mathcal{M}|^2 \rangle &= \frac{1}{2 \cdot 2} \frac{1}{8 \cdot 8} (\mathcal{M}_t + \mathcal{M}_u + \mathcal{M}_s + \mathcal{M}_{4g})_{\mu_1 \mu_2 \mu_3 \mu_4} (\mathcal{M}_t^* + \mathcal{M}_u^* + \mathcal{M}_s^* + \mathcal{M}_{4g}^*)_{\mu'_1 \mu'_2 \mu'_3 \mu'_4} \\
&\quad \times \mathcal{P}^{\mu_1 \mu'_1}(p_1) \times \mathcal{P}^{\mu_2 \mu'_2}(p_2) \times \mathcal{P}^{\mu_3 \mu'_3}(p_3) \times \mathcal{P}^{\mu_4 \mu'_4}(p_4),
\end{aligned} \tag{2.10}$$

where the averaging factors 2 and 8 are the numbers of gluon polarisation states and colours, correspondingly. The polarisation tensors \mathcal{P} , which take only the physical transverse polarisation states of the gluons into account, are in the covariant gauge (see Appendix A.2) [5, ch. 5.3][7, ch. 16.1]

$$\mathcal{P}^{\mu_1 \mu'_1}(p_1) = \sum_{\lambda_1} \epsilon_{\lambda_1}^{\mu_1}(p_1) \epsilon_{\lambda_1}^{* \mu'_1}(p_1) = -g^{\mu_1 \mu'_1} + \frac{p_1^{\mu_1} \tilde{p}_1^{\mu'_1} + \tilde{p}_1^{\mu_1} p_1^{\mu'_1}}{p_1 \cdot \tilde{p}_1}, \tag{2.11}$$

where $\tilde{p}_1 = (|\mathbf{p}_1|, -\mathbf{p}_1) \stackrel{\text{CMS}}{=} p_2$, $\tilde{p}_2 \stackrel{\text{CMS}}{=} p_1$, $\tilde{p}_3 \stackrel{\text{CMS}}{=} p_4$, and $\tilde{p}_4 \stackrel{\text{CMS}}{=} p_3$, and CMS here stands for centre of momentum frame of the colliding gluons.

Using the formulae given here one can directly calculate the invariant amplitude of the process $g + g \rightarrow g + g$ without the need of adding the Faddeev-Popov ghosts explicitly into the calculation (the ghost method can be seen for example in Risto Paatelainen's Master's thesis [12] and originally in [14]). The calculation itself would be very demanding with pen and paper, due to the excessive amount of terms in products. However, by using symbolical calculation on Wolfram Mathematica platform with excellent open source packages FeynCalc [15, 16] and FeynArts [17], the calculation can be made straightforwardly.

In my research training report [1], I went through the symbolical calculation of all the processes in Table 2.1. In addition, I calculated the full gluonic process $g + g \rightarrow g + g$ also in a general covariant gauge and in an axial gauge. All the source codes of these calculations are given in [18].

In a general axial gauge the gauge field A^μ needs to satisfy the gauge condition $n_\mu A^\mu = 0$ for some arbitrary four-vector n_μ . In this gauge the polarisation vector of a gluon can be shown to fulfil the conditions $n \cdot \epsilon(k) = 0$ and $k \cdot \epsilon(k) = 0$. With these the polarisation tensor \mathcal{P} can be shown to be (see Appendix A.3)

$$\mathcal{P}^{\mu\nu}(k) = -g^{\mu\nu} + \frac{n^\mu k^\nu + k^\mu n^\nu}{n \cdot k} - \frac{n^2 k^\mu k^\nu}{(n \cdot k)^2}. \tag{2.12}$$

In [1] I calculated the process $g + g \rightarrow g + g$ in a special case of this gauge with extra conditions $n^2 = 0$ and $\lambda = 0$. The n -vector can and even must be chosen separately for each external gauge field. For example, if for each external leg one

chooses $n = \tilde{p}$, the polarisation tensor simplifies into the form in (2.11). In the end, due to the gauge invariance of $\langle |\mathcal{M}|^2 \rangle$, all choices need to lead to the same result.

2.2 Integrated dijet production cross-section

The full integrated inclusive dijet production cross-section $\sigma^{p+p \rightarrow \text{j}et + \text{j}et + X} \equiv \sigma_{\text{j}et}(\sqrt{s}, k_0)$ in leading order can be found by integrating Equation (2.6) over the phase space $\Omega(\sqrt{s}, k_0)$ as follows:

$$\sigma_{\text{j}et}(\sqrt{s}, k_0) = \sum_{i,j,k,l} \int_{\Omega(\sqrt{s}, k_0)} dk_T^2 dy_1 dy_2 \frac{1}{1 + \delta_{kl}} x_1 f_i(x_1, Q^2) \cdot x_2 f_j(x_2, Q^2) \cdot \frac{d\hat{\sigma}^{ij \rightarrow kl}}{d\hat{t}}, \quad (2.13)$$

where $k_0 \gg \Lambda_{\text{QCD}}$ is some lower limit for k_T . The factor $\frac{1}{1 + \delta_{kl}}$ prevents the double counting of the phase space for identical final state particles.

The phase space region $\Omega(\sqrt{s}, k_0)$ in Equation (2.13) can be determined from the kinematical limitation that $x_1, x_2 \leq 1$. Using this and the Equations (2.7) and (2.8), one can show that

$$k_0 \leq k_T \leq \frac{\sqrt{s}}{2}, \quad (2.14)$$

$$|y_1| \leq \text{arcosh} \left(\frac{\sqrt{s}}{2k_T} \right) = \log \left(\frac{\sqrt{s}}{2k_T} + \sqrt{\frac{s}{4k_T^2} - 1} \right) \quad \text{and} \quad (2.15)$$

$$-\log \left(\frac{\sqrt{s}}{k_T} - e^{-y_1} \right) \leq y_2 \leq \log \left(\frac{\sqrt{s}}{k_T} - e^{y_1} \right). \quad (2.16)$$

This phase space region is illustrated in Figure 2.3 for y_1 and y_2 , keeping k_T fixed.

The summation in Equations (2.4), (2.6), and (2.13) must include all possible initial partons i and j , and all partonic subprocesses shown in Table 2.1. The Equation (2.13) written explicitly takes the form (denoting $x_1 f_g(x_1, Q^2) \equiv g_1$ and

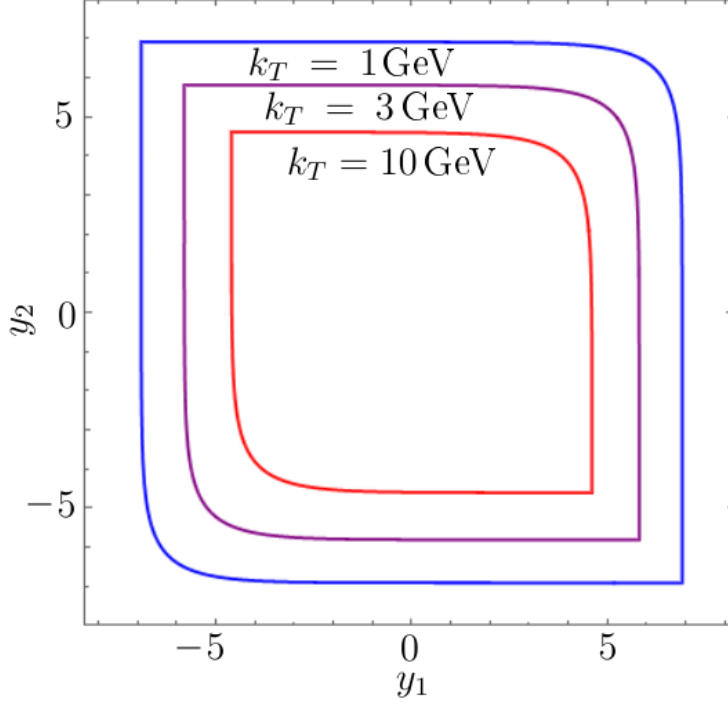


Figure 2.3: Plot of the shape of the limits of y_1 and y_2 in Equations (2.15) and (2.16) for three different values $k_T = 1$ GeV (blue curve), $k_T = 3$ GeV (purple curve), and $k_T = 10$ GeV (red curve). Here $\sqrt{s} = 1$ TeV.

other parton flavours similarly, for brevity)

$$\begin{aligned}
\sigma_{\text{jet}}(\sqrt{s}, k_0) = & \int_{\Omega(\sqrt{s}, k_0)} dk_T^2 dy_1 dy_2 \left\{ g_1 \cdot g_2 \cdot \frac{1}{2} \frac{d\hat{\sigma}^{gg \rightarrow gg}}{d\hat{t}} + g_1 \cdot g_2 \cdot \sum_{q=u,d,s,\dots} \frac{d\hat{\sigma}^{gg \rightarrow q\bar{q}}}{d\hat{t}} \right. \\
& + g_1 \cdot \sum_q q_2 \cdot \frac{d\hat{\sigma}^{gq \rightarrow gq}}{d\hat{t}} + g_1 \cdot \sum_{\bar{q}} \bar{q}_2 \cdot \frac{d\hat{\sigma}^{g\bar{q} \rightarrow g\bar{q}}}{d\hat{t}} \\
& + g_2 \cdot \sum_q q_1 \cdot \frac{d\hat{\sigma}^{qg \rightarrow qg}}{d\hat{t}} + g_2 \cdot \sum_{\bar{q}} \bar{q}_1 \cdot \frac{d\hat{\sigma}^{\bar{q}g \rightarrow \bar{q}g}}{d\hat{t}} \\
& + \sum_q q_1 \cdot q_2 \cdot \frac{1}{2} \frac{d\hat{\sigma}^{qq \rightarrow qq}}{d\hat{t}} + \sum_{\bar{q}} \bar{q}_1 \cdot \bar{q}_2 \cdot \frac{1}{2} \frac{d\hat{\sigma}^{\bar{q}\bar{q} \rightarrow \bar{q}\bar{q}}}{d\hat{t}} \\
& + \sum_{q,q',q \neq q'} q_1 \cdot q'_2 \cdot \frac{d\hat{\sigma}^{qq' \rightarrow qq'}}{d\hat{t}} + \sum_{\bar{q},\bar{q}',\bar{q} \neq \bar{q}'} \bar{q}_1 \cdot \bar{q}'_2 \cdot \frac{d\hat{\sigma}^{\bar{q}\bar{q}' \rightarrow \bar{q}\bar{q}'}}{d\hat{t}} \\
& + \left(\sum_q q_1 \right) \cdot \left(\sum_{\bar{q}',q \neq q'} \bar{q}'_2 \right) \cdot \frac{d\hat{\sigma}^{q\bar{q}' \rightarrow q\bar{q}'}}{d\hat{t}} + \left(\sum_{\bar{q}} \bar{q}_1 \right) \cdot \left(\sum_{q',q \neq q'} q'_2 \right) \cdot \frac{d\hat{\sigma}^{\bar{q}q' \rightarrow \bar{q}q'}}{d\hat{t}} \\
& + \sum_q q_1 \cdot \bar{q}_2 \cdot \left[\frac{d\hat{\sigma}^{q\bar{q} \rightarrow q\bar{q}}}{d\hat{t}} + \frac{1}{2} \frac{d\hat{\sigma}^{q\bar{q} \rightarrow gg}}{d\hat{t}} + \sum_{q' \neq q} \frac{d\hat{\sigma}^{q\bar{q} \rightarrow q'\bar{q}'}}{d\hat{t}} \right] \\
& \left. + \sum_{\bar{q}} \bar{q}_1 \cdot q_2 \cdot \left[\frac{d\hat{\sigma}^{\bar{q}q \rightarrow \bar{q}q}}{d\hat{t}} + \frac{1}{2} \frac{d\hat{\sigma}^{\bar{q}q \rightarrow gg}}{d\hat{t}} + \sum_{q' \neq q} \frac{d\hat{\sigma}^{\bar{q}q \rightarrow \bar{q}'q'}}{d\hat{t}} \right] \right\}, \quad (2.17)
\end{aligned}$$

which we will from now on call full partonic bookkeeping. The parton level Mandelstam variables in the subprocess cross-sections can be calculated using the formulae [2]

$$\hat{s}(k_T^2, y_1, y_2) = 2k_T^2(1 + \cosh(y_1 - y_2)), \quad (2.18)$$

$$\hat{t}(k_T^2, y_1, y_2) = -k_T^2(1 + e^{-(y_1 - y_2)}), \quad (2.19)$$

$$\hat{u}(k_T^2, y_1, y_2) = -k_T^2(1 + e^{+(y_1 - y_2)}), \quad (2.20)$$

where $\hat{u} = (x_1 h_1 - k_2)^2$, and we see that in the massless-parton limit discussed here we have $\hat{s} + \hat{t} + \hat{u} = 0$.

As Equation (2.17) is lengthy, it is often advantageous to use the so-called single effective subprocess (SES) approximation [2, 19, 20, 21] for first estimates. This approximation is based on the notice that, at high energies, processes with same initial and final partons ($gg \rightarrow gg$ and $gq \rightarrow gq$ in particular) dominate jet production. Equation (2.17) can be written as

$$\begin{aligned} \sigma_{\text{jet}}(\sqrt{s}, k_0) &= \int_{\Omega(\sqrt{s}, k_0)} dk_T^2 dy_1 dy_2 F(x_1, x_2, \hat{s}, \hat{t}, \hat{u}) \\ &= \frac{1}{2} \left[\int_{\Omega(\sqrt{s}, k_0)} dk_T^2 dy_1 dy_2 F(x_1, x_2, \hat{s}, \hat{t}, \hat{u}) + \int_{\Omega} dk_T^2 dy_1 dy_2 F(x_1, x_2, \hat{s}, \hat{t}, \hat{u}) \right]. \end{aligned} \quad (2.21)$$

Now make a note that the kinematic limits of y_1 and y_2 in Figure 2.3 are symmetric under exchange of y_1 and y_2 . Using Equations (2.7), (2.8), (2.18), (2.19), and (2.20), changing $y_1 \rightarrow y_2$, $y_2 \rightarrow y_1$ changes $x_1 \rightarrow x_1$, $x_2 \rightarrow x_2$, $\hat{s} \rightarrow \hat{s}$, $\hat{t} \rightarrow \hat{u}$ and $\hat{u} \rightarrow \hat{t}$. Making this exchange to the latter integral in (2.21) and then re-labeling the integration variables yields

$$\begin{aligned} \sigma_{\text{jet}} &= \frac{1}{2} \left[\int_{\Omega(\sqrt{s}, k_0)} dk_T^2 dy_1 dy_2 F(x_1, x_2, \hat{s}, \hat{t}, \hat{u}) + \int_{\Omega} dk_T^2 dy_2 dy_1 F(x_1, x_2, \hat{s}, \hat{u}, \hat{t}) \right] \\ &= \frac{1}{2} \left[\int_{\Omega(\sqrt{s}, k_0)} dk_T^2 dy_1 dy_2 F(x_1, x_2, \hat{s}, \hat{t}, \hat{u}) + \int_{\Omega} dk_T^2 dy_1 dy_2 F(x_1, x_2, \hat{s}, \hat{u}, \hat{t}) \right] \\ &= \frac{1}{2} \int_{\Omega(\sqrt{s}, k_0)} dk_T^2 dy_1 dy_2 [F(x_1, x_2, \hat{s}, \hat{t}, \hat{u}) + F(x_1, x_2, \hat{s}, \hat{u}, \hat{t})] \end{aligned}$$

$$\begin{aligned}
&= \frac{1}{2} \sum_{i,j,k,l} \int_{\Omega(\sqrt{s}, k_0)} dk_T^2 dy_1 dy_2 \\
&\quad x_1 f_i(x_1, Q^2) \cdot x_2 f_j(x_2, Q^2) \left[\frac{d\hat{\sigma}^{ij \rightarrow kl}}{d\hat{t}}(\hat{s}, \hat{t}, \hat{u}) + \frac{d\hat{\sigma}^{ij \rightarrow kl}}{d\hat{t}}(\hat{s}, \hat{u}, \hat{t}) \right] \frac{1}{1 + \delta_{kl}} \\
&= \frac{1}{2} \sum_{i,j,k,l} \int_{\Omega(\sqrt{s}, k_0)} dk_T^2 dy_1 dy_2 x_1 f_i(x_1, Q^2) \cdot x_2 f_j(x_2, Q^2) \left\langle \frac{d\hat{\sigma}^{ij \rightarrow kl}}{d\hat{t}}(\hat{s}, \hat{t}, \hat{u}) \right\rangle_{\hat{u}, \hat{t}},
\end{aligned} \tag{2.22}$$

where $\left\langle \frac{d\hat{\sigma}^{ij \rightarrow kl}}{d\hat{t}}(\hat{s}, \hat{t}, \hat{u}) \right\rangle_{\hat{u}, \hat{t}}$ are now called \hat{u}, \hat{t} -symmetrised cross-sections, and

$$\left\langle \frac{d\hat{\sigma}^{ij \rightarrow kl}}{d\hat{t}}(\hat{s}, \hat{t}, \hat{u}) \right\rangle_{\hat{u}, \hat{t}} = \begin{cases} \frac{d\hat{\sigma}^{ij \rightarrow kl}}{d\hat{t}}(\hat{s}, \hat{t}, \hat{u}) & \text{if } k = l \\ \frac{d\hat{\sigma}^{ij \rightarrow kl}}{d\hat{t}}(\hat{s}, \hat{t}, \hat{u}) + \frac{d\hat{\sigma}^{ij \rightarrow kl}}{d\hat{t}}(\hat{s}, \hat{u}, \hat{t}) & \text{if } k \neq l \end{cases}. \tag{2.23}$$

Now using Table 2.1 it is straightforward to show that one can estimate

$$\frac{\left\langle \frac{d\hat{\sigma}^{gq \rightarrow gq}}{d\hat{t}}(\hat{s}, \hat{t}, \hat{u}) \right\rangle_{\hat{u}, \hat{t}}}{\left\langle \frac{d\hat{\sigma}^{gg \rightarrow gg}}{d\hat{t}}(\hat{s}, \hat{t}, \hat{u}) \right\rangle_{\hat{u}, \hat{t}}} \approx \frac{4}{9}, \tag{2.24}$$

$$\frac{\left\langle \frac{d\hat{\sigma}^{qq \rightarrow qq}}{d\hat{t}}(\hat{s}, \hat{t}, \hat{u}) \right\rangle_{\hat{u}, \hat{t}}}{\left\langle \frac{d\hat{\sigma}^{gg \rightarrow gg}}{d\hat{t}}(\hat{s}, \hat{t}, \hat{u}) \right\rangle_{\hat{u}, \hat{t}}} \approx \left(\frac{4}{9} \right)^2, \tag{2.25}$$

where q can now be any quark or antiquark. Figure 2.4 illustrates this approximation. Now neglecting the effects of subprocesses that do not have same initial and final state particles, and using (2.24) and (2.25), Equation (2.22) simplifies into

$$\sigma_{\text{jet}} \approx \frac{1}{2} \int_{\Omega} dk_T^2 dy_1 dy_2 x_1 F_{\text{SES}}(x_1, Q^2) \cdot x_2 F_{\text{SES}}(x_2, Q^2) \cdot \frac{d\hat{\sigma}^{gg \rightarrow gg}}{d\hat{t}}, \tag{2.26}$$

where

$$F_{\text{SES}}(x, Q^2) = f_g(x, Q^2) + \frac{4}{9} \sum_{q=u,d,s,\dots} \left[f_q(x, Q^2) + f_{\bar{q}}(x, Q^2) \right]. \tag{2.27}$$

In what follows, in the minijet eikonal model considered here, $\sigma_{\text{jet}}(\sqrt{s}, k_0)$ is the key QCD quantity. We will consider k_0 as a parameter that needs to be fitted from experimental data. This parameter effectively sets the boundary between the perturbatively calculable hard subprocesses and the nonperturbative soft subprocesses. We will also see that, pushing pQCD validity to its limits, we should take k_0 to be of the order of few GeV. Jets of such a small transverse momenta ($p_T \leq 5$ GeV) are dubbed minijets as they cannot be observed directly as jets.

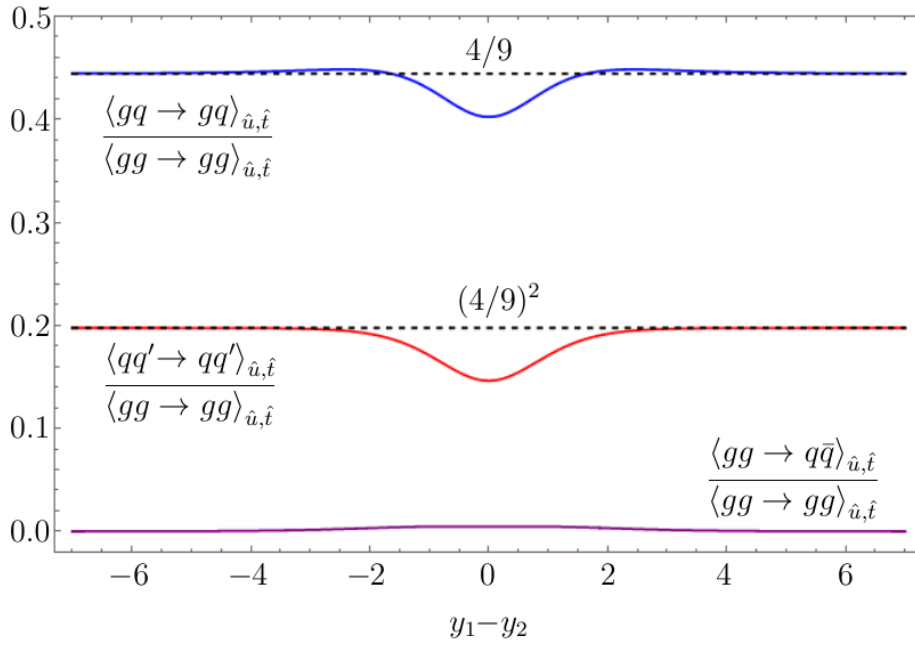


Figure 2.4: The $y_1 - y_2$ dependence of the \hat{u}, \hat{t} -symmetrised cross-sections of the processes $qg \rightarrow qg$, $qq' \rightarrow qq'$, and $gg \rightarrow q\bar{q}$, normalized to the cross-section of the process $gg \rightarrow gg$, calculated using the subprocess cross-sections in Table 2.1 and Equations (2.18)–(2.20). Notice that process $gg \rightarrow q\bar{q}$, where initial and final states are not same, is negligible.

Chapter 3

Eikonal approximation

In this chapter, we will derive the eikonal model for a non-relativistic quantum potential scattering problem. The derivation will follow Barone's and Predazzi's textbook [22] but is given here in more detail.

Scattering events can be classified into two categories. In elastic scattering, the final state particles are the same as the initial state particles, and in inelastic scattering, the particles change in the process. The elastic quantum scattering problem has a very precise classical analogy in the Kirchhoff's diffraction theory. In quantum world light waves are replaced by particles' wave functions and the hole in the screen is replaced by some scattering potential. The inelastic scattering also bears similarities to the classical diffraction theory in the case of perfectly absorptive interaction, but this analogy has its challenges (see discussion in [22, 23]).

3.1 Solving Schrödinger equation

Let us consider a particle scattering off a potential $V(\mathbf{r})$ that describes some kind of an interaction that has a limited range. We are interested in the high-energy limit so that particle energy dominates over the interaction potential,

$$E \gg |V(\mathbf{r})|. \quad (3.1)$$

For processes of interest, we can also make the assumption that our particle wavelength λ is much smaller than the interaction range a , i.e.

$$\lambda \ll a \iff ka \gg 1, \quad (3.2)$$

where $k = 2\pi/\lambda$ is the wave number of the particle. Effects of spin are neglected here, i.e. we consider only scattering of scalar particles. If we assume a stationary state, the particle is represented in coordinate space by its wave function $\psi(\mathbf{r})$ with location vector $\mathbf{r} = (x, y, z) \in \mathbb{R}^3$. The wave function is a solution to the non-relativistic time-independent Schrödinger Equation [24, p.144]

$$-\frac{\hbar^2}{2\mu}\nabla^2\psi(\mathbf{r}) + V(\mathbf{r})\psi(\mathbf{r}) = E\psi(\mathbf{r}), \quad (3.3)$$

where ∇^2 is the Laplacian operator, \hbar is the reduced Planck constant and E and μ are the energy and the mass of the particle. Consider the particle coming in along the z -axis so that at the limit of $z \rightarrow -\infty$ it is completely unaffected by the potential $V(\mathbf{r})$. Taking into account that if the conditions (3.1) and (3.2) are satisfied the scattering will happen dominantly into the forward direction we can make a plane wave motivated ansatz:

$$\psi(\mathbf{r}) = \phi(\mathbf{r})e^{i\mathbf{k}\cdot\mathbf{r}}, \quad (3.4)$$

where $\mathbf{k} = (0, 0, k) \in \mathbb{R}^3$ is the wave vector of the incoming wave and the modulation $\phi(\mathbf{r})$ is an unknown scalar field with boundary condition

$$\phi(x, y, -\infty) = 1, \quad (3.5)$$

so that $\psi(x, y, -\infty) = e^{ikz}$ i.e. an incoming plane wave.

Remembering De Broglie relation for particle momentum $\mathbf{p} = \hbar\mathbf{k}$ and that kinetic energy $E = \frac{\mathbf{p}^2}{2\mu}$ we denote $\frac{2\mu}{\hbar}E = k^2$. With this and by naming $U(\mathbf{r}) \equiv \frac{2\mu}{\hbar}V(\mathbf{r})$, Equation (3.3) simplifies to

$$[\nabla^2 - U(\mathbf{r}) + k^2] \psi(\mathbf{r}) = 0. \quad (3.6)$$

Substituting now our modulated plane wave solution from Equation (3.4) into Equation (3.6) we can derive a necessary condition for the function $\phi(\mathbf{r})$:

$$\begin{aligned} 0 &= [\nabla^2 - U(\mathbf{r}) + k^2] \phi(\mathbf{r})e^{i\mathbf{k}\cdot\mathbf{r}} \\ &= \nabla^2 (\phi(\mathbf{r})e^{i\mathbf{k}\cdot\mathbf{r}}) - U(\mathbf{r})\phi(\mathbf{r})e^{i\mathbf{k}\cdot\mathbf{r}} + k^2\phi(\mathbf{r})e^{i\mathbf{k}\cdot\mathbf{r}} \\ &= (\nabla^2\phi(\mathbf{r})) e^{i\mathbf{k}\cdot\mathbf{r}} + (2i\mathbf{k} \cdot \nabla\phi(\mathbf{r})) e^{i\mathbf{k}\cdot\mathbf{r}} - U(\mathbf{r})\phi(\mathbf{r})e^{i\mathbf{k}\cdot\mathbf{r}} \\ \iff 0 &= [\nabla^2 + 2i\mathbf{k} \cdot \nabla - U(\mathbf{r})] \phi(\mathbf{r}), \end{aligned} \quad (3.7)$$

where now $\mathbf{k} \cdot \nabla = k\partial_z$.

If we now assume that on the scale of $1/k$ the behaviour of the wave function ψ is

dominated by the exponential part, so that the function ϕ is essentially a constant, we can neglect the term $\nabla^2\phi$ in (3.7). Therefore we can separate

$$\begin{aligned} 2ik\partial_z\phi(x, y, z) &= U(x, y, z)\phi(x, y, z) \\ \iff \frac{\partial_z\phi(x, y, z)}{\phi(x, y, z)} &= -\frac{i}{2k}U(x, y, z). \end{aligned} \quad (3.8)$$

Integrating both sides of Equation (3.8) with respect to z and using the boundary condition (3.5) we get to a form

$$\begin{aligned} \int_1^\phi \frac{d\phi'}{\phi'} &= -\frac{i}{2k} \int_{-\infty}^z U(x, y, z') dz' \\ \iff \phi(x, y, z) &= \exp \left[-\frac{i}{2k} \int_{-\infty}^z U(x, y, z') dz' \right]. \end{aligned} \quad (3.9)$$

By substituting Equation (3.9) to our original ansatz (3.4) we can form the wave function

$$\psi(x, y, z) = \exp \left[ikz - \frac{i}{2k} \int_{-\infty}^z U(x, y, z') dz' \right]. \quad (3.10)$$

Let us still express the location vector by

$$\mathbf{r} \equiv \mathbf{b} + z\hat{\mathbf{e}}_z, \quad (3.11)$$

where $\hat{\mathbf{e}}_z$ is the z -direction unit vector and $\mathbf{b} = (x, y, 0) \in \mathbb{R}^3$ is called the impact parameter. With this definition, we get a solution

$$\psi(\mathbf{r}) = \exp \left[i\mathbf{k} \cdot \mathbf{r} - \frac{i}{2k} \int_{-\infty}^z U(\mathbf{b}, z') dz' \right] \quad (3.12)$$

for the outgoing wave.

3.2 Solving scattering amplitude

Let us now assume that asymptotically far away from the scattering centre, that is $|\mathbf{r}| \equiv r \rightarrow \infty$, the wave function of the system can be expressed as a superposition of the incoming plane wave and an outgoing spherical wave originating from the scattering centre. This can be written as

$$\psi(\mathbf{r}) \sim e^{i\mathbf{k}\cdot\mathbf{r}} + f(\mathbf{k}, \mathbf{k}') \frac{e^{ikr}}{r}, \quad \text{as } r \rightarrow \infty, \quad (3.13)$$

where $\mathbf{k}' \equiv |\mathbf{k}'|\hat{\mathbf{e}}_{\mathbf{r}}$ is the wave vector of the outgoing wave (see Figure 3.1) for which the conservation of energy necessitates that $|\mathbf{k}'| = |\mathbf{k}| = k$, and $f(\mathbf{k}, \mathbf{k}')$ is called scattering amplitude, and it depends only on the scattering angles (θ, ϕ) and the wave vector, $f(\mathbf{k}, \mathbf{k}') = f_{\mathbf{k}}(\theta, \phi)$. The scattering amplitude is a function of great interest, as it contains all the information of the scattering process.

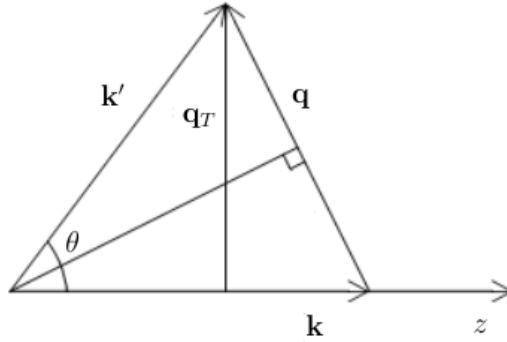


Figure 3.1: Illustration of how \mathbf{k} , $\mathbf{k}' \equiv |\mathbf{k}'|\hat{\mathbf{e}}_{\mathbf{r}}$, $\mathbf{q} \equiv \mathbf{k}' - \mathbf{k}$, and \mathbf{q}_T relate to each other, and to the scattering angle θ .

With the asymptotic behaviour of the wave function in Equation (3.13), the Schrödinger Equation (3.3) can be written as an integral Equation [24, p.424]:

$$\psi(\mathbf{r}) = e^{i\mathbf{k}\cdot\mathbf{r}} - \frac{1}{4\pi} \int \frac{e^{ik|\mathbf{r}-\mathbf{r}'|}}{|\mathbf{r}-\mathbf{r}'|} U(\mathbf{r}')\psi(\mathbf{r}') d^3\mathbf{r}'. \quad (3.14)$$

Taylor expanding the term $|\mathbf{r} - \mathbf{r}'|$ around the limit $\mathbf{r}' = \mathbf{0}$ (keeping the limit $\mathbf{r}' \ll \mathbf{r} \rightarrow \infty$ and the finite range of $U(\mathbf{r}')$ in mind) we find that

$$|\mathbf{r} - \mathbf{r}'| = r - \frac{\mathbf{r}' \cdot \mathbf{r}}{r} + \mathcal{O}(r^{-1}). \quad (3.15)$$

Inserting the expansion (3.15) to the integral Equation (3.14) we get

$$\begin{aligned}\psi(\mathbf{r}) &= e^{i\mathbf{k}\cdot\mathbf{r}} - \frac{1}{4\pi} \int \frac{e^{ik\left(r - \frac{\mathbf{r}'\cdot\mathbf{r}}{r} + \mathcal{O}(r^{-1})\right)}}{r - \frac{\mathbf{r}'\cdot\mathbf{r}}{r} + \mathcal{O}(r^{-1})} U(\mathbf{r}')\psi(\mathbf{r}') d^3\mathbf{r}' \\ &= e^{i\mathbf{k}\cdot\mathbf{r}} + \frac{e^{ikr}}{r} \left[\frac{-1}{4\pi} \int \frac{e^{-ik\frac{\mathbf{r}'\cdot\mathbf{r}}{r}}}{\left(1 - \frac{\mathbf{r}'\cdot\mathbf{r}}{r^2} + \mathcal{O}(r^{-2})\right)} e^{\mathcal{O}(r^{-1})} U(\mathbf{r}')\psi(\mathbf{r}') d^3\mathbf{r}' \right].\end{aligned}\quad (3.16)$$

In the asymptotic limit $r \rightarrow \infty$ we have $e^{\mathcal{O}(r^{-1})} \rightarrow 1$ and $-\frac{\mathbf{r}'\cdot\mathbf{r}}{r^2} + \mathcal{O}(r^{-2}) \rightarrow 0$. Now note that we can identify $\mathbf{k}' = k\frac{\mathbf{r}'}{r}$ and write

$$-ik\frac{\mathbf{r}'\cdot\mathbf{r}}{r} = -i\mathbf{k}'\cdot\mathbf{r}'.$$

Inserting these results into Equation (3.16) we arrive into

$$\lim_{r \rightarrow \infty} \psi(\mathbf{r}) = e^{i\mathbf{k}\cdot\mathbf{r}} + \left[\frac{-1}{4\pi} \int e^{-i\mathbf{k}'\cdot\mathbf{r}'} U(\mathbf{r}')\psi(\mathbf{r}') d^3\mathbf{r}' \right] \frac{e^{ikr}}{r}.\quad (3.17)$$

Comparing now Equations (3.13) and (3.17) we can read off the scattering amplitude as

$$f(\mathbf{k}, \mathbf{k}') = \frac{-1}{4\pi} \int e^{-i\mathbf{k}'\cdot\mathbf{r}'} U(\mathbf{r}')\psi(\mathbf{r}') d^3\mathbf{r}'.\quad (3.18)$$

Let us now define the momentum transfer vector $\mathbf{q} \equiv \mathbf{k}' - \mathbf{k}$ as in Figure 3.1. Remembering our definition of the impact parameter \mathbf{b} in Equation (3.11) and using the solution (3.12), we can express the scattering amplitude (3.18) as

$$\begin{aligned}f(\mathbf{k}, \mathbf{k}') &= \frac{-1}{4\pi} \int e^{-i\mathbf{k}'\cdot\mathbf{r}'} U(\mathbf{r}') \exp \left[i\mathbf{k}\cdot\mathbf{r}' - \frac{i}{2k} \int_{-\infty}^{z'} U(\mathbf{b}', z'') dz'' \right] d^3\mathbf{r}' \\ &= \frac{-1}{4\pi} \int e^{-i\mathbf{k}'\cdot(\mathbf{b}'+z'\hat{\mathbf{e}}_z)} U(\mathbf{b}', z') e^{i\mathbf{k}\cdot(\mathbf{b}'+z'\hat{\mathbf{e}}_z)} \exp \left[-\frac{i}{2k} \int_{-\infty}^{z'} U(\mathbf{b}', z'') dz'' \right] d^2\mathbf{b}' dz' \\ &= \frac{-1}{4\pi} \int e^{-i\mathbf{q}\cdot(\mathbf{b}'+z'\hat{\mathbf{e}}_z)} U(\mathbf{b}', z') \exp \left[-\frac{i}{2k} \int_{-\infty}^{z'} U(\mathbf{b}', z'') dz'' \right] d^2\mathbf{b}' dz'.\end{aligned}\quad (3.19)$$

As stated in Chapter 3.1, when assumptions (3.1) and (3.2) are satisfied, the scattering happens dominantly into the forward direction. Because of this, $\mathcal{O}(\theta^2) \ll 1$,

and we can approximate

$$\begin{aligned}
\mathbf{q} \cdot \mathbf{r}' &= \mathbf{q} \cdot (\mathbf{b}' + z' \hat{\mathbf{e}}_z) = \mathbf{q} \cdot \mathbf{b}' + z' (\mathbf{k} - \mathbf{k}') \cdot \hat{\mathbf{e}}_z \\
&= \mathbf{q}_T \cdot \mathbf{b}' + z' k (1 - \cos \theta) = \mathbf{q}_T \cdot \mathbf{b}' + \mathcal{O}(\theta^2) \\
&\approx \mathbf{q}_T \cdot \mathbf{b}',
\end{aligned}$$

where \mathbf{q}_T is now a two-dimensional transverse vector as indicated in Figure 3.1. Noting also that

$$\begin{aligned}
&\frac{\partial}{\partial z} \exp \left[\frac{-i}{2k} \int_{-\infty}^z U(\mathbf{b}, z') dz' \right] = \exp \left[\frac{-i}{2k} \int_{-\infty}^z U(\mathbf{b}, z') dz' \right] \left(\frac{-i}{2k} U(\mathbf{b}, z) \right) \\
\Rightarrow \int_{-\infty}^{\infty} U(\mathbf{b}, z) \exp \left[\frac{-i}{2k} \int_{-\infty}^z U(\mathbf{b}, z') dz' \right] dz &= \int_{-\infty}^{\infty} i2k \frac{\partial}{\partial z} \exp \left[\frac{-i}{2k} \int_{-\infty}^z U(\mathbf{b}, z') dz' \right] dz \\
&= i2k \int_{z=-\infty}^{\infty} \exp \left[\frac{-i}{2k} \int_{-\infty}^z U(\mathbf{b}, z') dz' \right] = i2k \left(\exp \left[\frac{-i}{2k} \int_{-\infty}^{\infty} U(\mathbf{b}, z') dz' \right] - 1 \right)
\end{aligned}$$

Equation (3.19) can be simplified into

$$\begin{aligned}
f(\mathbf{k}, \mathbf{k}') &= \frac{ik}{2\pi} \int e^{-i\mathbf{q}_T \cdot \mathbf{b}'} \left(1 - e^{\frac{-i}{2k} \int_{-\infty}^{\infty} U(\mathbf{b}', z'') dz''} \right) d^2\mathbf{b}' \\
&= \frac{ik}{2\pi} \int e^{-i\mathbf{q}_T \cdot \mathbf{b}'} \left(1 - e^{i\chi(\mathbf{b}')} \right) d^2\mathbf{b}' \\
&= \frac{ik}{2\pi} \int e^{-i\mathbf{q}_T \cdot \mathbf{b}} \Gamma(\mathbf{b}) d^2\mathbf{b},
\end{aligned} \tag{3.20}$$

where, in the last term, we have dropped the primes for simplicity, and defined the eikonal function as

$$\chi(\mathbf{b}) \equiv \frac{-1}{2k} \int_{-\infty}^{\infty} U(\mathbf{b}, z) dz \tag{3.21}$$

and the profile function as

$$\Gamma(\mathbf{b}) \equiv 1 - e^{i\chi(\mathbf{b})}. \tag{3.22}$$

3.3 Scattering cross-sections

Let us consider a continuous stationary flux of particles into some target, where they either scatter or continue on their way. The flux Φ_A is the number of incoming particles per unit time and unit area, N_T stands for the number of target particles and n_S is the number of scattering events in a unit time. With these in mind, we can define the elastic scattering cross-section as

$$\sigma_{\text{el}} \equiv \frac{n_S}{\Phi_A N_T}. \quad (3.23)$$

The probability current density $\mathbf{j}(\mathbf{r})$ of a system with wave function $\psi(\mathbf{r})$ can be expressed as [24, p.23]

$$\mathbf{j}(\mathbf{r}) = -\frac{i\hbar}{2\mu} [\psi^*(\mathbf{r})\nabla\psi(\mathbf{r}) - \psi(\mathbf{r})\nabla\psi^*(\mathbf{r})] = \frac{\hbar}{\mu} \text{Im} [\psi^*(\mathbf{r})\nabla\psi(\mathbf{r})]. \quad (3.24)$$

This relates to quantities of our interest as the total number of particles scattered through a sphere with a normal vector $d\mathbf{S} = r^2 d\Omega \hat{\mathbf{e}}_{\mathbf{r}}$ can be calculated as the integral of probability current density $\mathbf{j}_{\text{scatt}}$ related to the scattering, i.e.

$$\int \mathbf{j}_{\text{scatt}}(\mathbf{r}) \cdot d\mathbf{S} = \int \mathbf{j}_{\text{scatt}}(\mathbf{r}) \cdot \hat{\mathbf{e}}_{\mathbf{r}} r^2 d\Omega \xrightarrow{r \rightarrow \infty} \frac{n_S}{N_T}, \quad (3.25)$$

where the last integral is over the solid angle Ω . In Chapter 3.2 we hypothesised that in the asymptotic limit of $r \rightarrow \infty$, the wave function $\psi(\mathbf{r})$ of our system can be expressed as a linear combination of incoming plane wave $\psi_{\text{inc}}(\mathbf{r})$ and scattered spherical wave $\psi_{\text{scatt}}(\mathbf{r})$ in the form of

$$\psi(\mathbf{r}) \sim e^{i\mathbf{k}\cdot\mathbf{r}} + f(\mathbf{k}, \mathbf{k}') \frac{e^{ikr}}{r} \equiv \psi_{\text{inc}}(\mathbf{r}) + \psi_{\text{scatt}}(\mathbf{r}), \quad \text{as } r \rightarrow \infty. \quad (3.26)$$

By substituting (3.26) into (3.24) we get

$$\begin{aligned} \mathbf{j}(\mathbf{r}) &\stackrel{r \rightarrow \infty}{\sim} \frac{\hbar}{\mu} \text{Im} \left[(\psi_{\text{inc}}^*(\mathbf{r}) + \psi_{\text{scatt}}^*(\mathbf{r})) \nabla (\psi_{\text{inc}}(\mathbf{r}) + \psi_{\text{scatt}}(\mathbf{r})) \right] \\ &= \frac{\hbar}{\mu} \text{Im} \left[\psi_{\text{inc}}^*(\mathbf{r}) \nabla \psi_{\text{inc}}(\mathbf{r}) + \psi_{\text{scatt}}^*(\mathbf{r}) \nabla \psi_{\text{scatt}}(\mathbf{r}) \right. \\ &\quad \left. + \left(\psi_{\text{inc}}^*(\mathbf{r}) \nabla \psi_{\text{scatt}}(\mathbf{r}) + \psi_{\text{scatt}}^*(\mathbf{r}) \nabla \psi_{\text{inc}}(\mathbf{r}) \right) \right] \\ &\equiv \mathbf{j}_{\text{inc}}(\mathbf{r}) + \mathbf{j}_{\text{scatt}}(\mathbf{r}) + \mathbf{j}_{\text{int}}(\mathbf{r}), \end{aligned} \quad (3.27)$$

where we have now identified the probability current densities related to incoming ($\mathbf{j}_{\text{inc}}(\mathbf{r})$) and scattered ($\mathbf{j}_{\text{scatt}}(\mathbf{r})$) waves and an interference term $\mathbf{j}_{\text{int}}(\mathbf{r})$. By looking

further into $\mathbf{j}_{\text{scatt}}(\mathbf{r})$, we find that

$$\begin{aligned}
\mathbf{j}_{\text{scatt}}(\mathbf{r}) \cdot \hat{\mathbf{e}}_{\mathbf{r}} &= \frac{\hbar}{\mu} \text{Im} [\psi_{\text{scatt}}^*(\mathbf{r}) \nabla \psi_{\text{scatt}}(\mathbf{r})] \cdot \hat{\mathbf{e}}_{\mathbf{r}} \\
&= \frac{\hbar}{\mu} \text{Im} \left[\left(f^*(\mathbf{k}, \mathbf{k}') \frac{e^{-ikr}}{r} \right) \hat{\mathbf{e}}_{\mathbf{r}} \cdot \nabla \left(f(\mathbf{k}, \mathbf{k}') \frac{e^{ikr}}{r} \right) \right] \\
&= \frac{\hbar}{\mu} \text{Im} \left[|f(\mathbf{k}, \mathbf{k}')|^2 \frac{e^{-ikr}}{r} ik \frac{e^{ikr}}{r} \right] - \frac{\hbar}{\mu} \text{Im} \left[\frac{|f(\mathbf{k}, \mathbf{k}')|^2}{r^3} \right] \\
\Rightarrow \quad \mathbf{j}_{\text{scatt}}(\mathbf{r}) \cdot \hat{\mathbf{e}}_{\mathbf{r}} &= \frac{\hbar k}{\mu r^2} |f(\mathbf{k}, \mathbf{k}')|^2. \tag{3.28}
\end{aligned}$$

Also noting that the incoming flux Φ_{A} simplifies to

$$\begin{aligned}
\Phi_{\text{A}} &= \lim_{r \rightarrow \infty} |\mathbf{j}_{\text{inc}}(\mathbf{r})| = \lim_{r \rightarrow \infty} \left| \frac{\hbar}{\mu} \text{Im} [\psi_{\text{inc}}^*(\mathbf{r}) \nabla \psi_{\text{inc}}(\mathbf{r})] \right| \\
&= \lim_{r \rightarrow \infty} \left| \frac{\hbar}{\mu} \text{Im} [e^{-i\mathbf{k} \cdot \mathbf{r}} \nabla e^{i\mathbf{k} \cdot \mathbf{r}}] \right| = \lim_{r \rightarrow \infty} \left| \frac{\hbar}{\mu} \text{Im} [e^{-ikz} \nabla e^{ikz}] \right| \\
&= \lim_{r \rightarrow \infty} \left| \frac{\hbar}{\mu} \text{Im} [ik e^{-ikz} e^{ikz} \hat{\mathbf{e}}_z] \right| \\
&= \frac{\hbar k}{\mu}, \tag{3.29}
\end{aligned}$$

we can write the elastic cross-section σ from Equation (3.23) as

$$\sigma_{\text{el}} = \frac{1}{\Phi_{\text{A}}} \frac{n_{\text{S}}}{N_{\text{T}}} = \lim_{r \rightarrow \infty} \frac{\mu}{\hbar k} \frac{\hbar k}{\mu} \int \frac{1}{r^2} |f(\mathbf{k}, \mathbf{k}')|^2 r^2 d\Omega = \int |f(\mathbf{k}, \mathbf{k}')|^2 d\Omega. \tag{3.30}$$

Taking a closer look at Equation (3.20) we find that

$$\begin{aligned}
f(\mathbf{k}, \mathbf{k}') &= f(\mathbf{q}_T) = \frac{ik}{2\pi} \int e^{-i\mathbf{q}_T \cdot \mathbf{b}} \Gamma(\mathbf{b}) d^2\mathbf{b} = ik2\pi \left[\frac{1}{(2\pi)^2} \int e^{-i\mathbf{q}_T \cdot \mathbf{b}} \Gamma(\mathbf{b}) d^2\mathbf{b} \right] \\
&= ik2\pi \mathcal{F}^{-1}(\Gamma)(\mathbf{q}_T), \tag{3.31}
\end{aligned}$$

or the scattering amplitude $f(\mathbf{q}_T)$ is a two-dimensional inverse Fourier transform of the profile function $\Gamma(\mathbf{b})$. Inverting this, the profile function can be expressed as a Fourier transform of the scattering amplitude, i.e.

$$\Gamma(\mathbf{b}) = \mathcal{F}(\mathcal{F}^{-1}(\Gamma))(\mathbf{b}) = \frac{-i}{2\pi k} \mathcal{F}(f)(\mathbf{b}) = \frac{-i}{2\pi k} \int e^{i\mathbf{q}_T \cdot \mathbf{b}} f(\mathbf{q}_T) d^2\mathbf{q}_T. \tag{3.32}$$

Parseval's theorem states that for a function g with a two-dimensional domain,

$$\int |g(\mathbf{q}_T)|^2 d^2\mathbf{q}_T = \frac{1}{(2\pi)^2} \int |\mathcal{F}(g)(\mathbf{b})|^2 d^2\mathbf{b} \tag{3.33}$$

holds. Lastly, we need to turn our attention to the differential forms. As can be

seen from Figure 3.1, the length of the transverse momentum transfer vector \mathbf{q}_T can be approximated with

$$q_T \equiv |\mathbf{q}_T| = k \sin \theta \approx k\theta, \quad (3.34)$$

where $\theta \in [0, \pi]$, the angle between the momentum vectors \mathbf{k} and \mathbf{k}' , is assumed to be small. Now using Equation (3.34) the differential form $d\mathbf{q}_T$ can be expressed in polar coordinates and with the solid angle Ω approximatively as

$$d^2\mathbf{q}_T = q_T dq_T d\phi \approx (k\theta)d(k\theta)d\phi \approx k^2 \sin \theta d\theta d\phi = k^2 d \cos \theta d\phi = k^2 d\Omega. \quad (3.35)$$

Finally combining our Equations (3.31), (3.32), (3.33), and (3.35) into Equation (3.30), we find that the elastic scattering cross-section in the eikonal model is

$$\begin{aligned} \sigma_{\text{el}} &= \int |f(\mathbf{q})|^2 d\Omega = (2\pi)^2 \int |\mathcal{F}^{-1}(\Gamma)(\mathbf{q}_T)|^2 k^2 \frac{1}{k^2} d^2\mathbf{q}_T \\ &= (2\pi)^2 \frac{1}{(2\pi)^2} \int |\mathcal{F}(\mathcal{F}^{-1}(\Gamma))(\mathbf{b})|^2 d^2\mathbf{b} \\ &= \int |\Gamma(\mathbf{b})|^2 d^2\mathbf{b} = \int |1 - e^{i\chi(\mathbf{b})}|^2 d^2\mathbf{b}. \end{aligned} \quad (3.36)$$

Optical theorem tells us that [24, ch. 11] the total cross-section σ_{tot} is proportional to the imaginary part of the scattering amplitude $f(\mathbf{q})$ in the forward scattering direction when $\mathbf{q} = \mathbf{q}_T = \mathbf{0}$, i.e.

$$\sigma_{\text{tot}} = \frac{4\pi}{k} \text{Im}(f(\mathbf{k}, \mathbf{k}' = \mathbf{k})). \quad (3.37)$$

Inserting Equation (3.20) into Equation (3.37) yields the total cross-section

$$\sigma_{\text{tot}} = \frac{4\pi}{k} \text{Im} \left(\frac{ik}{2\pi} \int \Gamma(\mathbf{b}) d^2\mathbf{b} \right) = 2 \int \text{Re}(1 - e^{i\chi(\mathbf{b})}) d^2\mathbf{b}. \quad (3.38)$$

The difference of the total cross-section σ_{tot} and the elastic cross-section σ_{el} is the inelastic cross-section σ_{in} . Subtracting (3.36) from (3.38) yields us

$$\begin{aligned} \sigma_{\text{in}} &= \sigma_{\text{tot}} - \sigma_{\text{el}} = \int [2\text{Re}\Gamma(\mathbf{b}) - |\Gamma(\mathbf{b})|^2] d^2\mathbf{b} \\ &= \int 2 [1 - \text{Re}(e^{i\text{Re}\chi(\mathbf{b}) - \text{Im}\chi(\mathbf{b})})] - [(\text{Re}\Gamma(\mathbf{b}))^2 + (\text{Im}\Gamma(\mathbf{b}))^2] d^2\mathbf{b} \\ &= \int 2 [1 - e^{-\text{Im}\chi(\mathbf{b})} \cos(\text{Re}\chi(\mathbf{b}))] - [1 - 2e^{-\text{Im}\chi(\mathbf{b})} \cos(\text{Re}\chi(\mathbf{b})) + e^{-2\text{Im}\chi(\mathbf{b})}] d^2\mathbf{b} \end{aligned}$$

$$\Rightarrow \quad \sigma_{\text{in}} = \int (1 - e^{-2\text{Im}\chi(\mathbf{b})}) d^2\mathbf{b}. \quad (3.39)$$

Thus, as expected, the inelastic cross-section follows (only) from the imaginary part of the eikonal function $\chi(\mathbf{b})$, i.e. (see Equation (3.21)) from the imaginary part of the scattering potential.

The Mandelstam variable t in the high energy limit with our notation can be expressed as $t \equiv (k_\mu - k'_\mu)^2 = (E - E')^2 - (\mathbf{k} - \mathbf{k}')^2 = -q_T^2 = -2k^2(1 - \cos\theta)$ [6], where k_μ and k'_μ are four-vectors and $E = E'$. Now reading from Equation (3.30) we can write the elastic differential cross-section

$$\begin{aligned} \frac{d\sigma_{\text{el}}}{d\Omega} &= \frac{d\sigma_{\text{el}}}{d\cos\theta d\phi} = \frac{dt}{d\cos\theta} \frac{d\sigma_{\text{el}}}{dt d\phi} = 2k^2 \frac{d\sigma_{\text{el}}}{dt d\phi} = |f(\mathbf{q}_T)|^2 \\ \Leftrightarrow \quad \frac{d\sigma_{\text{el}}}{dt} &= \frac{1}{2k^2} \int_0^{2\pi} |f(\mathbf{q}_T)|^2 d\phi = \pi \left| \frac{f(\mathbf{q}_T)}{k} \right|^2 \\ &= \pi \left| \frac{1}{2\pi} \int e^{-i\mathbf{q}_T \cdot \mathbf{b}} \Gamma(\mathbf{b}) d^2\mathbf{b} \right|^2 \\ &= \pi \left| \frac{1}{2\pi} \int_0^\infty \int_0^{2\pi} e^{-iq_T b \cos\theta} \Gamma(\mathbf{b}) b d\theta db \right|^2 \\ \Leftrightarrow \quad \frac{d\sigma_{\text{el}}}{dt} &= \pi \left| \int_0^\infty \Gamma(\mathbf{b}) J_0(b\sqrt{-t}) b db \right|^2, \end{aligned} \quad (3.40)$$

where we have used Equation (3.31) and the integral representation [22, Eq. 2.133]

$$J_0(x) = \frac{1}{2\pi} \int_0^{2\pi} e^{ix \cos\theta} d\theta \quad (3.41)$$

for the Bessel function J_0 .

Although the above results are derived from nonrelativistic Schrödinger Equation, they can be generalised for relativistic wave functions [22]. Notice that in Equation (3.40), the $\frac{d\sigma_{\text{el}}}{dt}$ is a fully Lorentz invariant quantity, so it directly generalises into the relativistic case. Integrating then yields straightforwardly Equation (3.36). Equation (3.38) can, again, be derived from the optical theorem. Then, exactly as we did above, Equation (3.39) can be obtained from Equations (3.36) and (3.38).

Chapter 4

Eikonal minijet model

In this Chapter we study the eikonal minijet model [25, 26]. We are interested in studying proton–proton collisions with the eikonal formalism discussed in Chapter 3. Consider the limit of small real part in the scattering potential, so that we have $i\chi(\mathbf{b}) \approx -\text{Im}\chi(\mathbf{b}) \equiv -\chi(b, s)$. Equations (3.36), (3.38), and (3.39) read now

$$\sigma_{\text{el}} = \pi \int_0^{\infty} (1 - e^{-\chi(b,s)})^2 db^2 \quad (4.1)$$

$$\sigma_{\text{in}} = \pi \int_0^{\infty} (1 - e^{-2\chi(b,s)}) db^2 \quad (4.2)$$

$$\sigma_{\text{tot}} = 2\pi \int_0^{\infty} (1 - e^{-\chi(b,s)}) db^2 \quad (4.3)$$

where the eikonal function $\chi(b, s)$, which is assumed to depend on the centre of momentum (CMS) energy (\sqrt{s}) of the collision, is now a real number, and we have used $d^2\mathbf{b} = \pi db^2$ which holds assuming azimuthal symmetry of cross-sections in impact parameter.

Now let us concentrate on the inelastic cross-section σ_{in} . The Equation (4.2) can be written as an integral of series

$$\begin{aligned} \sigma_{\text{in}} &= \pi \int_0^{\infty} (1 - e^{-2\chi(b,s)}) db^2 = \pi \int_0^{\infty} e^{-2\chi(b,s)} (e^{2\chi(b,s)} - 1) db^2 \\ &= \pi \int_0^{\infty} \sum_{n=1}^{\infty} \frac{(2\chi(b,s))^n}{n!} e^{-2\chi(b,s)} db^2 \equiv \pi \int_0^{\infty} \sum_{n=1}^{\infty} P_n(b,s) db^2, \end{aligned} \quad (4.4)$$

where we have now identified the Poissonian probability mass function $P_n(b, s)$, which corresponds to the probability of having n distinct events with the average number of events being $2\chi(b, s)$. These events are now perturbative (hard) and nonperturbative (soft) partonic collisions, which destroy the colliding protons. In this thesis, we will neglect the effect of soft processes [25], and assume that the (mini)jet production discussed in Chapter 2 is the sole contributor in σ_{in} bringing the transverse momentum cutoff k_0 to as small a value as possible. Then, $k_0 \sim \mathcal{O}(1 \text{ GeV})$ and we are indeed discussing minijets, the few-GeV partons, which are certainly present in the proton–proton collision although they cannot be directly observed. This leads us to interpret $P_n(b, s)$ as the probability of n independent minijet-producing collisions in an inelastic event, and thus we can assume

$$2\chi(b, s) = \sigma_{\text{jet}}(s, k_0)A(b), \quad (4.5)$$

where $\sigma_{\text{jet}}(s, k_0)$ is defined in Chapter 2 and $A(b)$ is the effective partonic overlap function of the protons at an impact parameter b . The function $A(b)$ is given by the convolution of the individual proton thickness functions T_n normalized to unity, i.e.

$$A(\mathbf{b}) = \int T_n(\mathbf{b}')T_n(\mathbf{b} - \mathbf{b}') d^2\mathbf{b}', \quad (4.6)$$

$$\int A(\mathbf{b}) d^2\mathbf{b} = 1, \quad \int T_n(\mathbf{b}) d^2\mathbf{b} = 1. \quad (4.7)$$

Since the minijet production considered here is dominated by gluonic subprocesses, the T_n above is to be understood as the gluonic thickness function. To obtain that, we first follow Ref. [27] and exploit the exclusive electroproduction of J/ψ at HERA, $\gamma^* + p \rightarrow J/\psi + p$, for which ZEUS has measured the differential cross section near $t = 0$ to be $\frac{d\sigma}{dt} \propto \exp(-b|t|) \propto |G|^2$ with a slope $b = (4.72 \pm 0.19) \text{ GeV}^2$ [28]. Taking a 2-dimensional Fourier transformation of the corresponding 2-gluon form factor G leads to a Gaussian distribution for T_n ,

$$T_n(\mathbf{b}) = \frac{1}{2\pi\sigma^2} e^{-\frac{\mathbf{b}^2}{2\sigma^2}}, \quad (4.8)$$

with a width parameter $\sigma = \sqrt{b} = 0.43 \text{ fm}$. Doing the integration in (4.6) in Cartesian coordinates gives us straightforwardly a Gaussian overlap

$$A(\mathbf{b}) = \frac{1}{4\pi\sigma^2} e^{-\frac{\mathbf{b}^2}{4\sigma^2}}. \quad (4.9)$$

With some algebraic modifications the integral representations of the inelastic and total cross-sections can be expressed with exponential integral functions [29, Ch.

5.1]:

$$\begin{aligned}
\sigma_{\text{in}} &= 4\pi\sigma^2 \int_0^{\frac{\sigma_{\text{jet}}}{4\pi\sigma^2}} (1 - e^{-t}) \frac{dt}{t} = 4\pi\sigma^2 \text{Ein}\left(\frac{\sigma_{\text{jet}}}{4\pi\sigma^2}\right) \\
&= 4\pi\sigma^2 \left(\gamma + \ln\left(\frac{\sigma_{\text{jet}}}{4\pi\sigma^2}\right) + \text{E}_1\left(\frac{\sigma_{\text{jet}}}{4\pi\sigma^2}\right) \right), \tag{4.10}
\end{aligned}$$

$$\begin{aligned}
\sigma_{\text{tot}} &= 8\pi\sigma^2 \int_0^{\frac{\sigma_{\text{jet}}}{8\pi\sigma^2}} (1 - e^{-t}) \frac{dt}{t} = 8\pi\sigma^2 \text{Ein}\left(\frac{\sigma_{\text{jet}}}{8\pi\sigma^2}\right) \\
&= 8\pi\sigma^2 \left(\gamma + \ln\left(\frac{\sigma_{\text{jet}}}{8\pi\sigma^2}\right) + \text{E}_1\left(\frac{\sigma_{\text{jet}}}{8\pi\sigma^2}\right) \right), \tag{4.11}
\end{aligned}$$

where $\gamma \approx 0.57722$ is the Euler–Mascheroni constant, and

$$\text{E}_1(z) = \int_z^\infty \frac{e^{-t}}{t} dt = -\gamma - \ln z - \sum_{k=1}^{\infty} \frac{(-z)^k}{k k!}. \tag{4.12}$$

Chapter 5

Numerical calculations

In this chapter, we will review the various numerical methods used in fitting the eikonal minijet model described in Chapter 4 to the experimental data on total cross-sections of proton–proton [30, 31, 32, 33, 34, 35] and proton–antiproton collisions [35]. All numerical calculations were written from scratch with C++, the code is available at [36].

5.1 Calculating cross-sections

The jet cross-section σ_{jet} was calculated via using both the full partonic bookkeeping (2.13) and the single effective subprocess approximation (2.26). The needed subprocess cross-sections were read from Table 2.1, and all variables were written in the (k_T^2, y_1, y_2) space using Equations (2.18)–(2.20) and (2.7)–(2.16). The PDFs were calculated with the LHAPDF [37] interpolating library using the leading or-

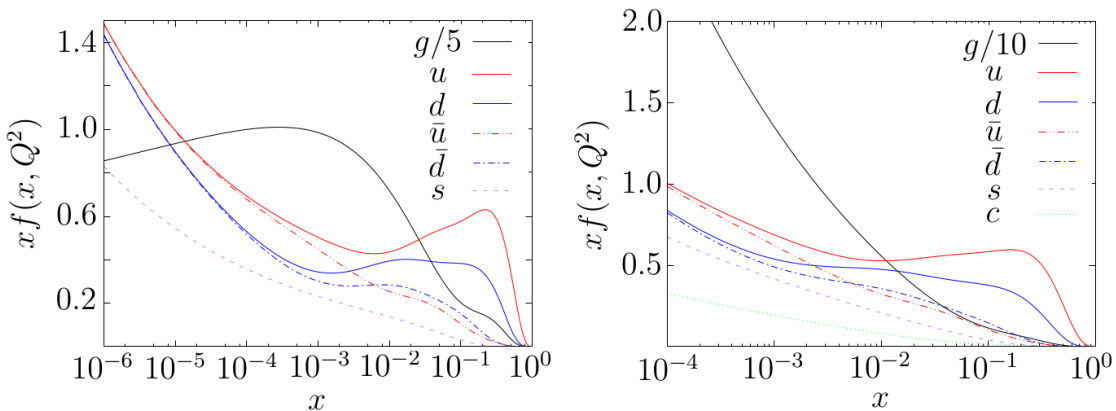


Figure 5.1: CT14LO [38] PDFs $xf(x, Q^2)$ as a function of momentum fraction x at $Q^2 = (1.3 \text{ GeV})^2$ (on left) and $Q^2 = 10 \text{ GeV}^2$ (on right). Notice the scalings for gluons.

der CT14LO PDF set [38]. This set also provided the coupling constant $\alpha_s(Q^2)$ as a function of transverse momentum, $Q^2 = k_T^2$. Illustration of the used PDFs is shown in Figure 5.1.

For numerical simplicity the integral was subjected to a standard transformation

$$\begin{aligned} & \int_{a_1}^{b_1} \int_{a_2(x_1)}^{b_2(x_1)} \int_{a_3(x_1, x_2)}^{b_3(x_1, x_2)} F(x_1, x_2, x_3) dx_1 dx_2 dx_3 \\ &= \int_0^1 \int_0^1 \int_0^1 F(x_1, x_2, x_3) (b_1 - a_1)(b_2 - a_2)(b_3 - a_3) dz_1 dz_2 dz_3, \end{aligned} \quad (5.1)$$

$$\text{where} \quad x_i = a_i + z_i(b_i - a_i).$$

The integral itself was then calculated using a recursive adaptive three dimensional integration algorithm implemented in the Cubature [39] library.

The total and inelastic cross-sections σ_{tot} and σ_{in} were calculated from σ_{jet} using Equations (4.10) and (4.11). The exponential integral functions were evaluated using their series representations implemented in the GSL [40] library. The elastic cross-section σ_{el} was then calculated by subtracting σ_{in} from σ_{tot} .

5.2 Fitting transverse momentum cutoff

The lower transverse momentum cutoff k_0 was chosen such that the calculated total cross-section σ_{tot} would coincide with the best fit to experimental data made by the COMPETE collaboration [41]. The fitting algorithm was based on the secant method: Two small initial trial values $x_0 \neq x_1$ were chosen for k_0 by trial and error such that the integral would converge. After the first two calculations of the total cross-section σ_{tot} , the new trial values x_i , $i = 2, 3, \dots$ would be calculated using recursive formula

$$x_i = \frac{x_{i-2} \sigma_{\text{err}}(x_{i-1}) - x_{i-1} \sigma_{\text{err}}(x_{i-2})}{\sigma_{\text{err}}(x_{i-1}) - \sigma_{\text{err}}(x_{i-2})}, \quad \sigma_{\text{err}}(k_0) \equiv \sigma_{\text{tot}}(k_0) - \sigma_{\text{data}}, \quad (5.2)$$

where σ_{data} would be the experimental data fit for the total cross-section at a given value of \sqrt{s} . This procedure would be then continued until $\sigma_{\text{err}}(k_0)$ would be satisfyingly close to zero. After this fitting of the cutoff momentum we would then have already calculated the corresponding $\sigma_{\text{jet}}(s, k_0)$, which could be further used to calculate σ_{in} and finally σ_{el} .

5.3 Contributions of multiple minijet production

As hinted before in Chapter 4, in the eikonal minijet model the inelastic cross-section σ_{in} can be interpreted as a sum of cross-sections that correspond to the probabilities of observing multiple independent minijet production events. This can be seen by writing the summation in Equation (4.4) explicitly:

$$\sigma_{\text{in}} = \pi \int_0^\infty \sum_{n=1}^\infty P_n(b, s) db^2 = \pi \int_0^\infty P_1 db^2 + \pi \int_0^\infty P_2 db^2 + \pi \int_0^\infty P_3 db^2 + \dots \quad (5.3)$$

In other words, σ_{in} is due to the cases where at least one minijet-pair is formed. This observation leads us to study the quantity

$$G_n(s, k_0) = \frac{\pi \int_0^\infty P_n db^2}{\sigma_{\text{in}}} = \frac{\pi}{\sigma_{\text{in}}} \int_0^\infty \frac{(\sigma_{\text{jet}}(s, k_0)A(b))^n}{n!} e^{-\sigma_{\text{jet}}(s, k_0)A(b)} db^2. \quad (5.4)$$

The value of $G_n \in [0, 1]$ thus denotes the contribution a single event with production of n pairs of minijets has on σ_{in} . It can also be interpreted as a probability that a single observed inelastic event corresponds to a production of n pairs of minijets. The values of G_n :s were obtained using adaptive integration routines in the GSL library [40].

5.4 Conservation of momentum?

If multiple independent minijet production indeed takes place in an inelastic proton–proton scattering, one could be concerned with the conservation of momentum. Breaking of this would be an obvious sign of violating the assumed independence of parton–parton collisions. Clearly, the sum of the momenta of the individual partons cannot exceed the initial momenta of the protons they are from. To take this effect into account for example in (5.4), one must limit the phase space of each subsequent calculation of σ_{jet} . In calculating G_n , we should then calculate the σ_{jet}^n in (5.4) as

$$\sigma_{\text{jet}}^n = \left(\prod_{\alpha=1}^n \int_{\Omega} dk_{T,\alpha}^2 dy_{1,\alpha} dy_{2,\alpha} F(k_{T,\alpha}^2, y_{1,\alpha}, y_{2,\alpha}) \right) \cdot \theta \left(1 - \sum_{\alpha=1}^n x_{1,\alpha} \right) \theta \left(1 - \sum_{\alpha=1}^n x_{2,\alpha} \right), \quad (5.5)$$

where θ is the Heaviside step function, and x_1 and x_2 depend on the integral variables via (2.7) and (2.8). The integration limits in (5.5) are now mutually dependent, so the integrals cannot be calculated separately, but as a one, $3n$ -dimensional integral. As the dimensionality of the integrals increases so rapidly, Monte Carlo methods are needed to solve Equation (5.5) numerically. We also note that the factor

$$e^{-\sigma_{\text{jet}}(s,k_0)A(b)} = \frac{1}{1 + \sigma_{\text{jet}}(s, k_0)A(b) + \frac{1}{2!}(\sigma_{\text{jet}}(s, k_0)A(b))^2 + \dots},$$

i.e. the probability for no minijet production, should also be modified accordingly, with $\sigma_{\text{jet}}^n(s, k_0)$ from Equation (5.5).

Chapter 6

Results

First, we wanted to estimate the error of using the single effective subprocess approximation described in Chapter 2 in calculating σ_{jet} . Figure 6.1 shows σ_{jet} calculated using both the full partonic bookkeeping and the SES approximation with a constant momentum cutoff $k_0 = 2 \text{ GeV}$. Next the same comparison was made by using the momentum cutoffs k_0 that were found by fitting the σ_{tot} to data,

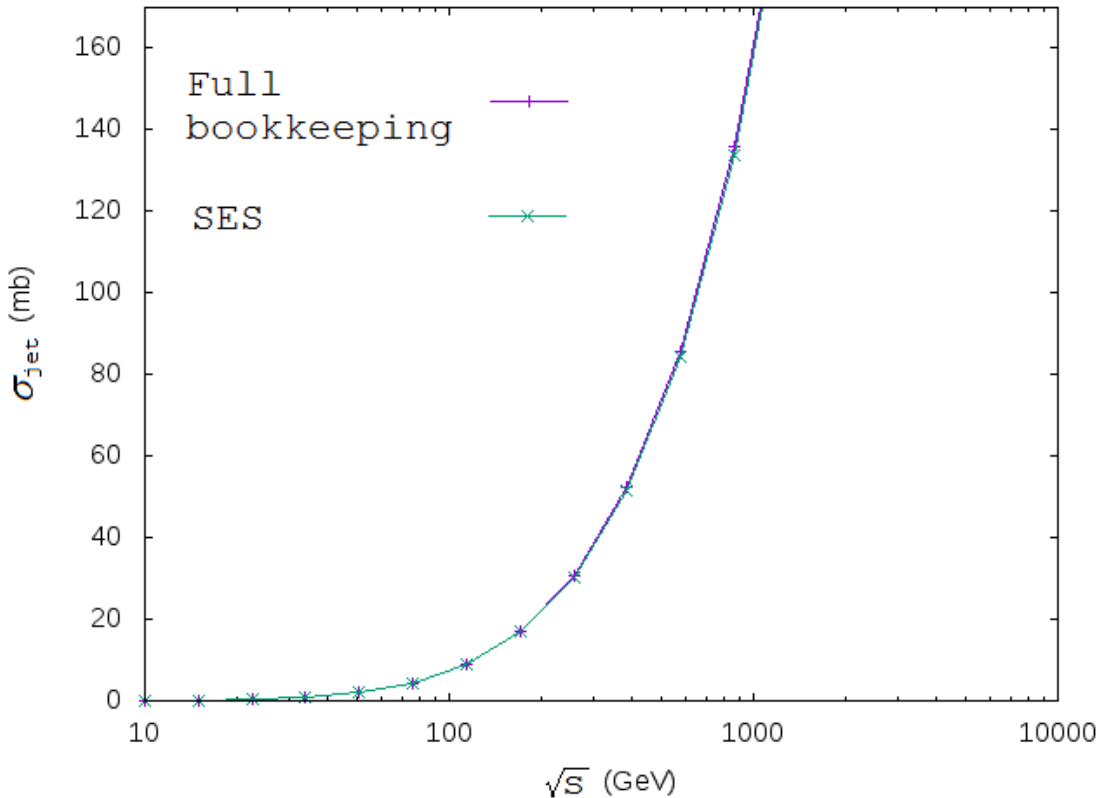


Figure 6.1: Minijet cross-section $\sigma_{\text{jet}}(s, k_0)$ calculated as a function of CMS energy \sqrt{s} in leading order pQCD, with a constant momentum cutoff $k_0 = 2 \text{ GeV}$, and computed with the full bookkeeping (2.17) and the SES approximation (2.26).

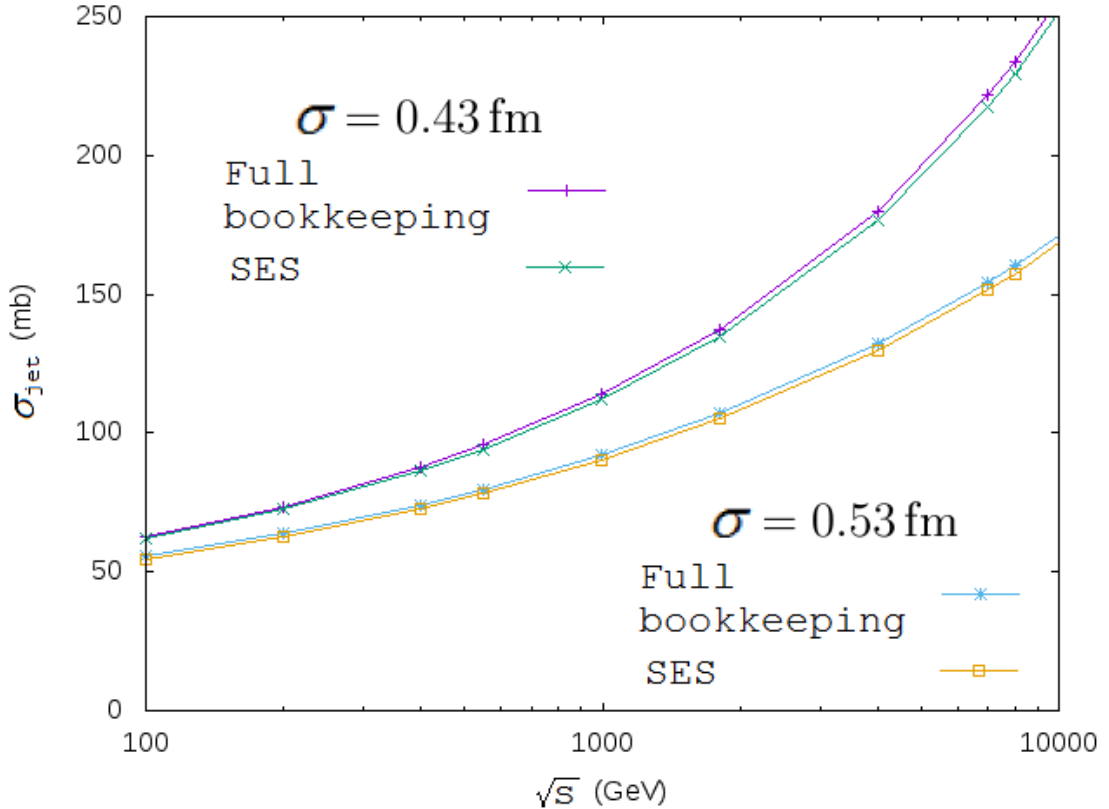


Figure 6.2: Jet cross-section $\sigma_{\text{jet}}(s, k_0(\sqrt{s}))$ calculated as a function of CMS energy \sqrt{s} in leading order pQCD, with a momentum cutoff $k_0(\sqrt{s})$ such that σ_{tot} fits to data (see Figure 6.5).

as explained in Section 5.1. The results of the latter calculation are represented in Figure 6.2. Both Figures 6.1 and 6.2 show a minuscule relative error in using SES approximation, it undershoots the value of σ_{jet} by at most 1.8% in the \sqrt{s} -range studied. The relative error tolerance of the integration routine was 10^{-4} , so the difference cannot be explained just due to numerical inaccuracy.

The SES approximation is based on the assumption that processes $gg \rightarrow gg$ and $gq \rightarrow gq$ dominate the minijet production. These subprocess cross-sections have largest values, as can be seen from Figure 2.4. The subprocess cross-sections are, in Equation (2.17), weighted by partonic luminosities $x_1 f_i(x_1, Q^2) x_2 f_j(x_2, Q^2)$. The gluonic PDFs have such high values at high energies (see Figure 5.1) that the gluonic processes clearly dominate over other processes. To demonstrate this effect, we calculated the luminosities $x_1 f_i(x_1, Q^2) x_2 f_j(x_2, Q^2)$ with $i = g, u$ and $j = g, u$ for values $\sqrt{s} = 1$ TeV and $k_T = 3$ GeV, as a function of rapidities y_1 and y_2 using Equations (2.7) and (2.8). The results are shown in Figure 6.3. The shape of the plots in this figure can be understood with the help of Figure 5.1: when $y_1 = y_2 = 0$, $x_1 = x_2 = \frac{2k_T}{\sqrt{s}} = 6 \cdot 10^{-3}$, where the gluonic PDFs have their global maximum, and up quark PDFs have a local minimum. Moving in any direction from this point decreases gluonic PDFs' values, hence the lone peak

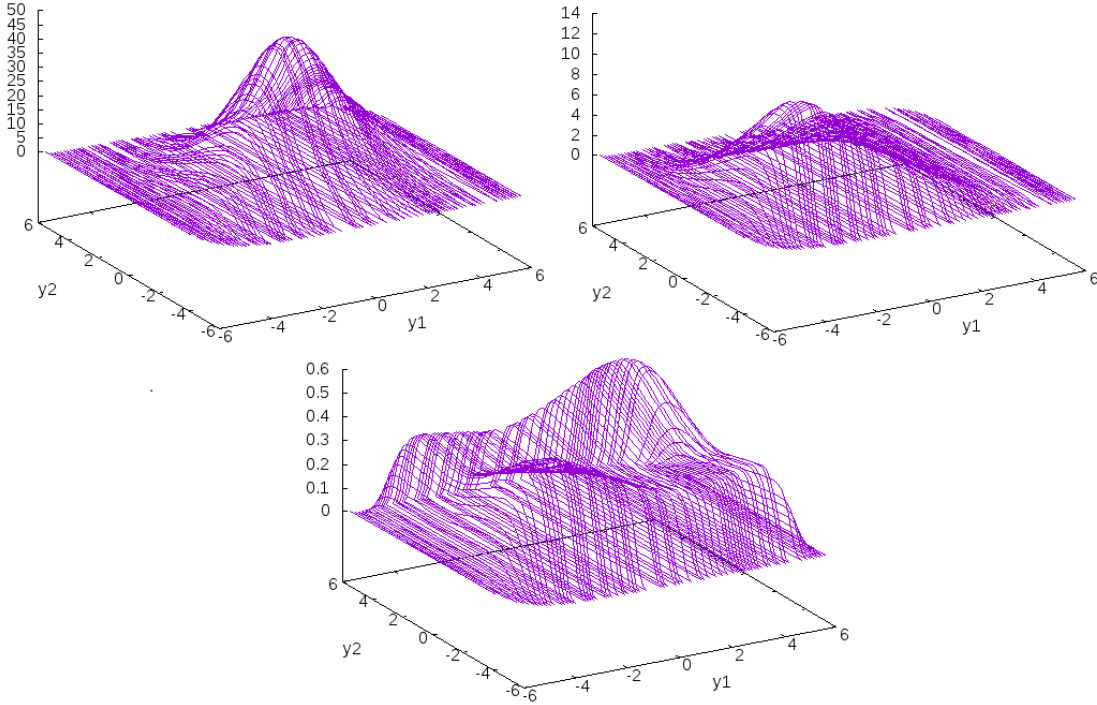


Figure 6.3: Parton luminosities $x_1 f_g(x_1, Q^2) x_2 f_g(x_2, Q^2)$ (top left picture), $x_1 f_g(x_1, Q^2) x_2 f_u(x_2, Q^2)$ (top right picture), and $x_1 f_u(x_1, Q^2) x_2 f_u(x_2, Q^2)$ (bottom picture) calculated with CT14LO [38] PDFs, at $\sqrt{s} = 1$ TeV and $k_T = 3$ GeV, as a function of rapidities y_1 and y_2 using Equations (2.7) and (2.8).

in $x_1 f_g(x_1, Q^2) x_2 f_g(x_2, Q^2)$. The Equations (2.7) and (2.8) are symmetric with respect to exchanging y_1 and y_2 , and $x_1 f_u(x_1, Q^2) x_2 f_u(x_2, Q^2)$ is symmetric with respect to exchange of x_1 and x_2 . In the positive quadrant, both quark PDF terms grow to form a peak, as x_1 grows from the PDF's local minimum and x_2 shrinks. In the quadrant where y_1 grows and y_2 shrinks (or other way around), both x_1 and x_2 grow and form a peak at the quark PDF's local maximum. The plot of the mixed term $x_1 f_g(x_1, Q^2) x_2 f_u(x_2, Q^2)$ follows the gluonic PDF's form as it has much higher values than the up quark PDF. Overall, from the Figure 6.3 we can clearly see that gluonic subprocesses' cross-sections get a very dominant weight in the whole integral domain in Equation (2.17). These two effects combined lead to the dominance of the processes $gg \rightarrow gg$ and $gq \rightarrow gq$ over all the others in the minijet production. To further demonstrate this effect, we calculated the fractional contribution from each subprocess of Table 2.1 to σ_{jet} . These results are shown in Figure 6.4, from which we can read that the gluon dominance is very clear at high energies.

After these calculations, we fitted the total cross-section σ_{tot} to the best fit of experimental data [41]:

$$\sigma_{\text{tot, fit}}^{\bar{p}p, pp}(s) = 42.6 (s)^{-0.46} \pm 33.4 (s)^{-0.545} + 0.307 \log^2 \left(\frac{s}{29.1} \right) + 35.5$$

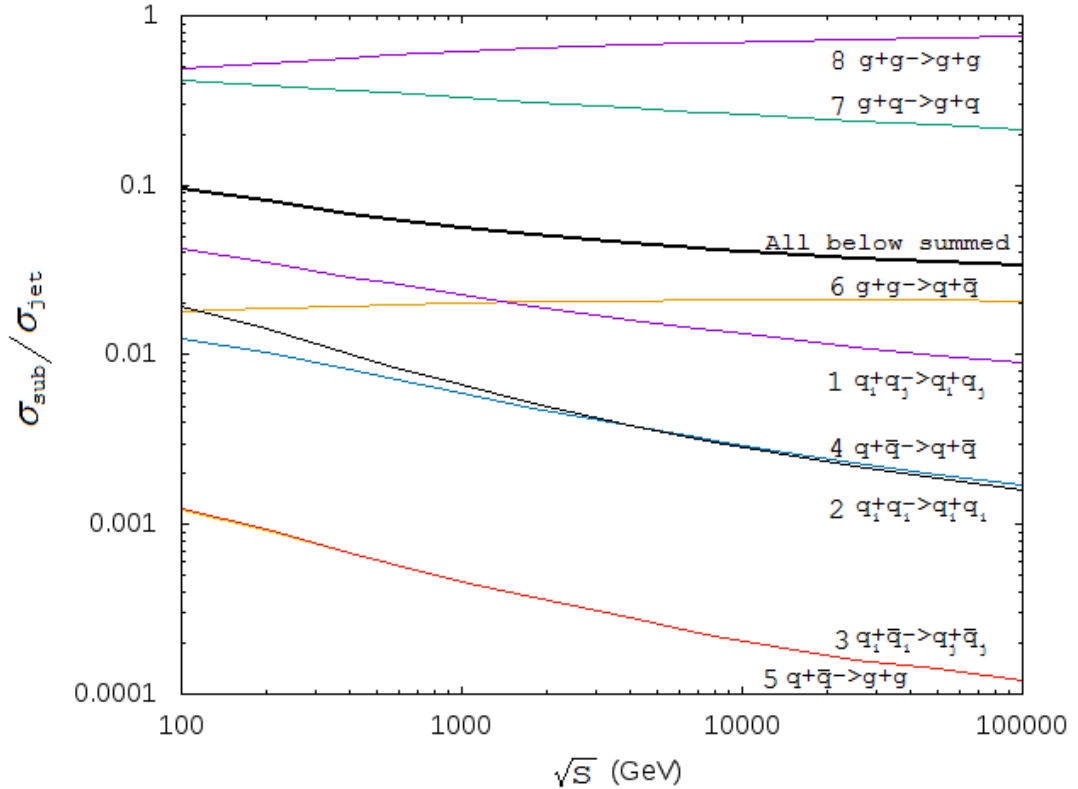


Figure 6.4: The contributions of individual subprocesses (see Table 2.1) to the minijet cross-section σ_{jet} calculated as a function of CMS energy \sqrt{s} in leading order pQCD, with a momentum cutoff k_0 such that σ_{tot} fits to data (see Figure 6.5). Each σ_{sub} is calculated otherwise exactly like σ_{jet} , but with setting all other subprocess cross-sections to zero than the subprocess in question.

using the momentum cutoff k_0 in $\sigma_{\text{jet}}(\sqrt{s}, k_0)$ as a fitting parameter. The procedure is explained in Section 5.2. The fitted k_0 as a function of the CMS energy \sqrt{s} is represented in Figure 6.5. The data points fell somewhat on a straight line on a log-log plot, suggesting that the momentum cutoff is ruled by a power law $k_0 \propto (\sqrt{s})^{0.19}$. Interestingly, this behaviour is qualitatively similar to what is predicted in the pQCD saturation model [42].

Next, we proceeded to calculate the cross-sections σ_{in} and σ_{el} using the obtained momentum cutoffs (Figure 6.5) as explained in Chapter 5.1. The results are shown in Figure 6.6. From these, we can see that, when the Gaussian width $\sigma = 0.43$ fm and when the model parameter k_0 is tuned so that σ_{tot} fits the experimental data, the eikonal minijet model slightly undershoots the inelastic cross-section σ_{in} .

In the results calculated with $\sigma = 0.43$ fm in Figure 6.6, the problem is in the proportionality of σ_{in} and σ_{el} with respect to σ_{tot} . Therefore, this problem cannot be corrected by simply taking higher order pQCD corrections into σ_{jet} , as this would generally just raise the value of σ_{jet} . As can be seen from Equations (4.1), (4.2), and (4.3), raising the value of σ_{jet} (thus raising the value of χ) leads into

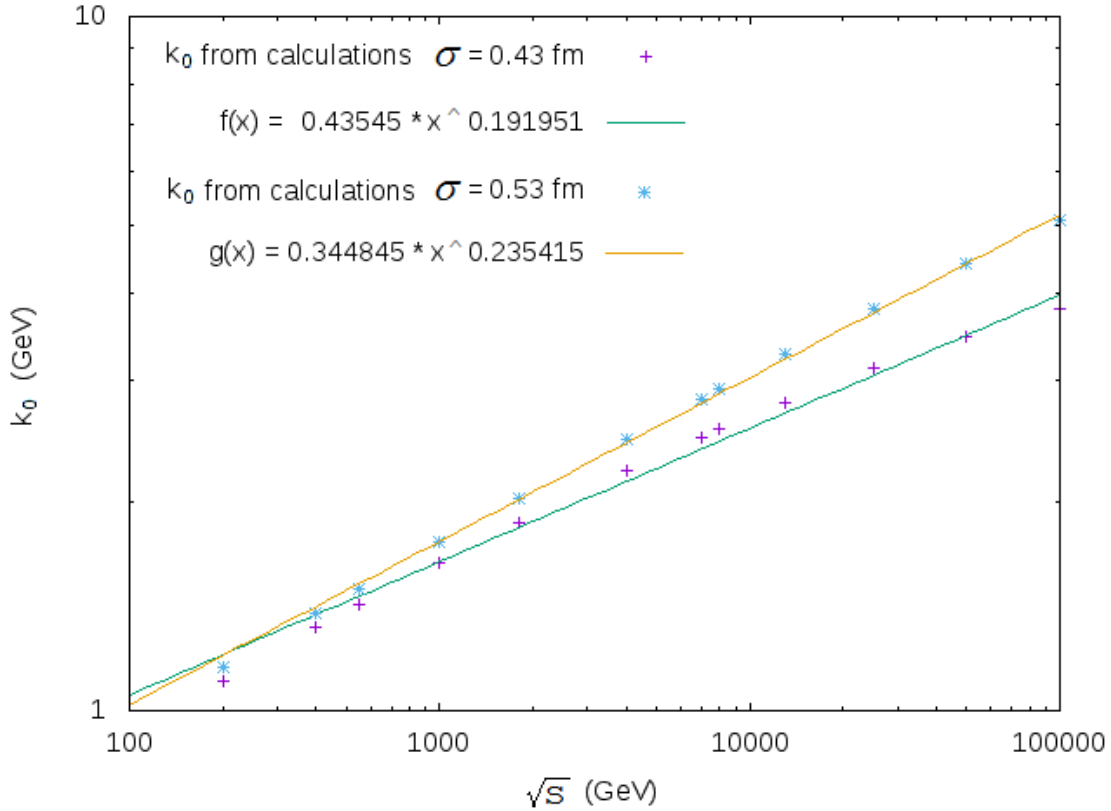


Figure 6.5: The fitted momentum cutoff k_0 as a function of CMS energy \sqrt{s} , from fitting the total cross-section σ_{tot} to the experimental data with width parameters $\sigma = 0.43$ (crosses and the green curve) and $\sigma = 0.53$ (stars and the orange curve). The fitting procedure is explained in detail in Section 5.2. Notice the power-law-like behaviour.

raising values of all three cross-sections, σ_{in} , σ_{el} , and σ_{tot} , not into lowering σ_{el} while raising σ_{in} and keeping σ_{tot} still, which would be needed. As a matter of fact, the contributions of higher order pQCD corrections have already been effectively taken into account by the fitting of k_0 , because it forces the σ_{jet} to take the appropriate value, no matter what terms lie in it.

Another modification one could make to the eikonal minijet model would be to allow for a real part in χ , i.e. considering also purely elastic events. As can be seen from Equation (3.39), this would keep the value of σ_{in} unchanged, but, as can be seen from Equations (3.36) and (3.38), raise both σ_{tot} and σ_{el} , thus making the proportionality issue even worse.

To understand the effect of the width of the proton thickness function T_n on the ratios $\frac{\sigma_{\text{in}}}{\sigma_{\text{tot}}}$ and $\frac{\sigma_{\text{el}}}{\sigma_{\text{tot}}}$, let us consider a toy model, where T_n is such that the partonic overlap function A in Equation (4.6) becomes the Heaviside θ in the

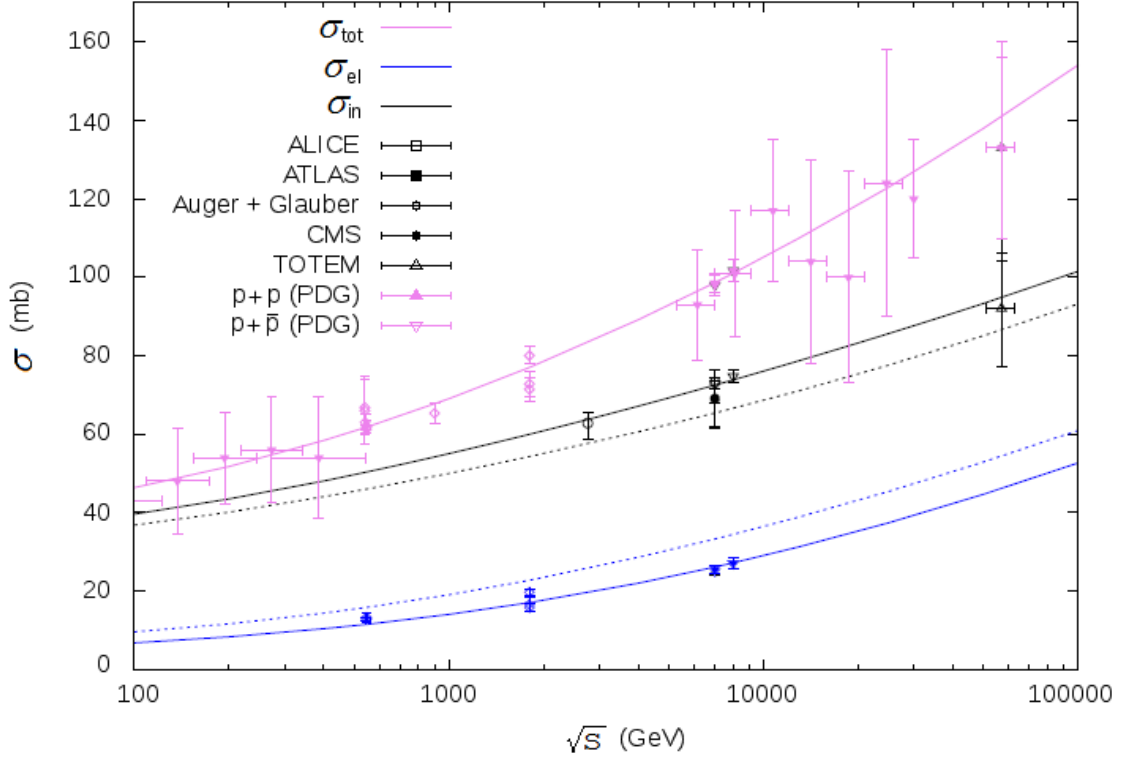


Figure 6.6: The calculated cross-sections σ_{tot} (pink curve), σ_{in} (black curves), and σ_{el} (blue curves) as functions of CMS energy \sqrt{s} . The solid lines are calculated using width parameter $\sigma = 0.53$ fm and the dotted lines using $\sigma = 0.43$ fm. The experimental data is from [30, 31, 32, 33, 34, 35].

radial direction:

$$A(\mathbf{b}) = \frac{1}{\pi\sigma^2}\theta(\sigma - b) \quad \int A(\mathbf{b}) d^2\mathbf{b} = 1. \quad (6.1)$$

Clearly, as can be seen from the Gaussian A , the width parameter σ here is in direct correlation with that in T_n . Inserting this overlap function into the eikonal minijet model, Equations (4.1), (4.2), and (4.3) yield straightforwardly ratios

$$\frac{\sigma_{\text{in}}}{\sigma_{\text{tot}}} = \frac{1}{2}(1 + e^{-\frac{\sigma_{\text{jet}}(s, k_0)}{2\pi\sigma^2}}) \quad \text{and} \quad (6.2)$$

$$\frac{\sigma_{\text{el}}}{\sigma_{\text{tot}}} = \frac{1}{2}(1 - e^{-\frac{\sigma_{\text{jet}}(s, k_0)}{2\pi\sigma^2}}). \quad (6.3)$$

From these, we directly see that in order to raise $\frac{\sigma_{\text{in}}}{\sigma_{\text{tot}}}$ and lower $\frac{\sigma_{\text{el}}}{\sigma_{\text{tot}}}$, one has to raise the width parameter σ relative to σ_{jet} . Then, since $\sigma_{\text{tot}} = \frac{\sigma_{\text{jet}}}{x}(1 - e^{-x})$, where $x = \frac{\sigma_{\text{jet}}}{2\pi\sigma^2}$, we can see that the lowering of x must be compensated with the lowering of σ_{jet} to keep σ_{tot} unchanged.

We found by the method of trial and error that raising the width parameter σ of the proton thickness functions T_n to a value of $\sigma = 0.53$ fm fits our model very well with the experimental data. Very interestingly, this value also nearly fits the

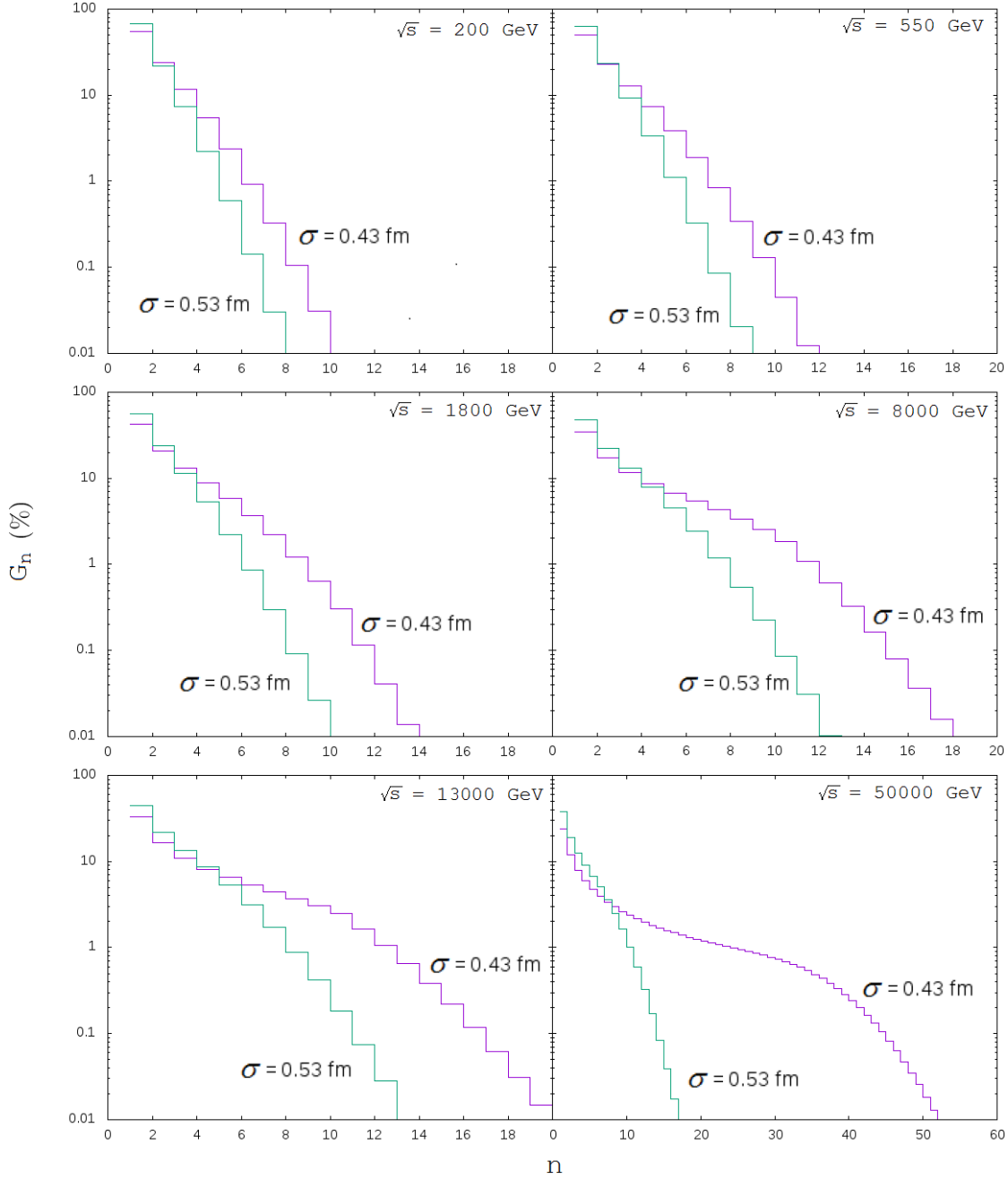


Figure 6.7: Probabilities G_n of the production of n jets for CMS energies $\sqrt{s} = 200$ GeV, 550 GeV, 1800 GeV, 8000 GeV, 13000 GeV, and 50000 GeV with width parameters $\sigma = 0.43$ fm (purple curves) and $\sigma = 0.53$ fm (green curves).

error margins of the value $\sigma = (0.43 \pm 0.09)$ fm obtained from Ref. [28]. The cross-sections calculated with $\sigma = 0.53$ fm are also shown in Figures 6.2 and 6.6, and the re-fitted k_0 is represented in Figure 6.5.

Next we calculated the probabilities G_n of the production of n pairs of minijets for some selected values of \sqrt{s} for both values $\sigma = 0.43$ fm and $\sigma = 0.53$ fm of the width parameter. The procedure used is explained in Section 5.3. The results are shown in Figure 6.7. As expected, at lower energies most of the inelastic collisions produce only one pair of minijets, and then as the energy grows, the

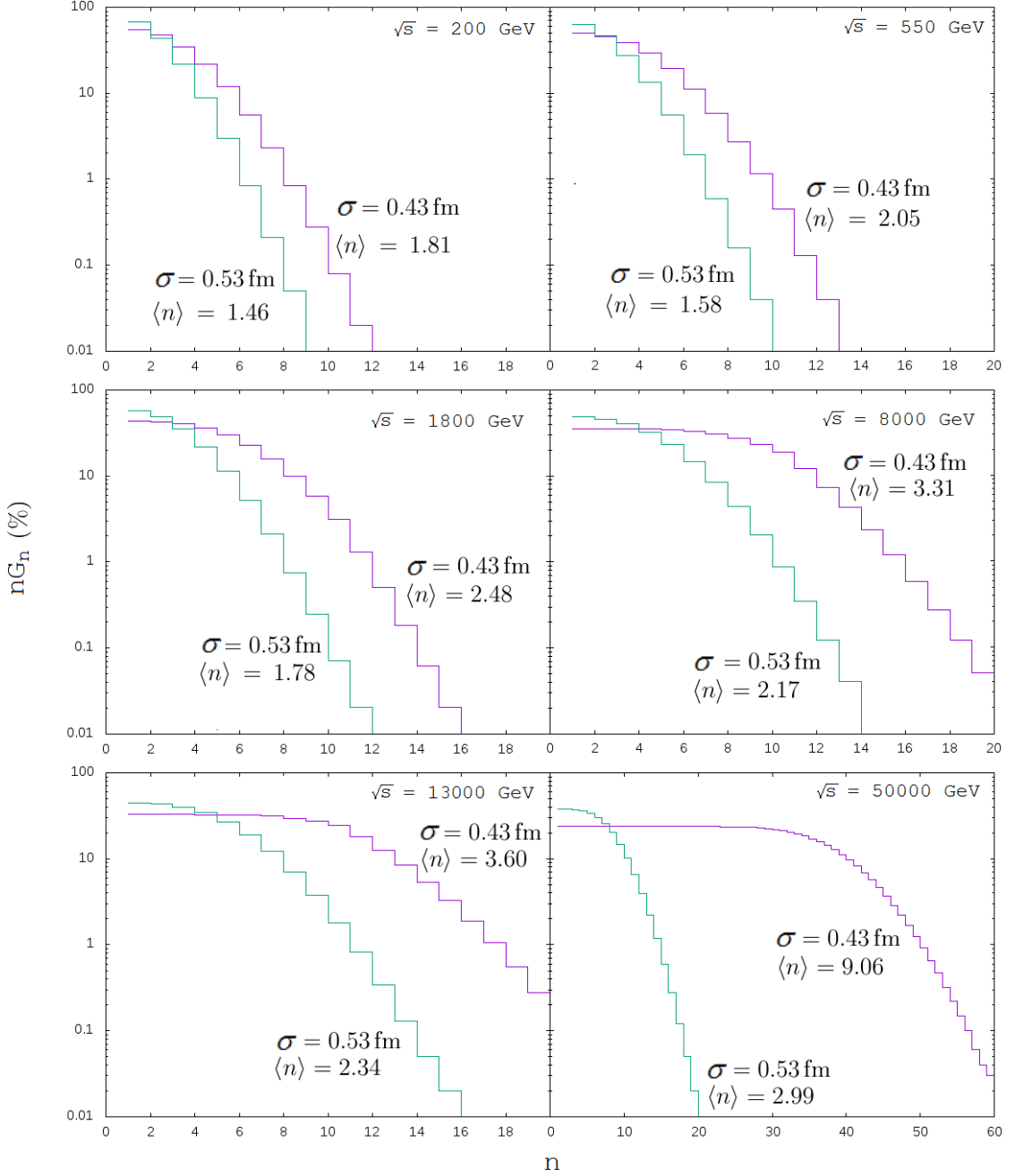


Figure 6.8: Probabilities G_n of the production of n jets, multiplied by n , for CMS energies $\sqrt{s} = 200$ GeV, 550 GeV, 1800 GeV, 8000 GeV, 13000 GeV, and 50000 GeV with width parameters $\sigma = 0.43$ fm (purple curves) and $\sigma = 0.53$ fm (green curves). In each plot there is also the quantities $\langle n \rangle = \sum_n n \cdot G_n$ given.

production of multiple pairs of minijets becomes more significant, while the one-pair production stays as the most probable one in all cases studied. There is, however, a significant difference in the results for different width parameter values. This is also reasonable, as can be seen from Figure 6.5, for narrower protons the fitting parameter k_0 is lower, leading to higher σ_{jet} , and higher probabilities for multiple minijet pairs produced. Looking at Figure 6.7 might be a bit misleading for intuition, as even though multiple minijet productions have low probability,

they produce indeed many pairs of minijets. This shifts our attention to the quantity $n \cdot G_n$, as the expected value of minijetpairs produced in a single inelastic proton–proton collision can be calculated as $\langle n \rangle = \sum_{n=1}^{\infty} n \cdot G_n = \frac{\sigma_{\text{jet}}}{\sigma_{\text{in}}}$. The quantities $n \cdot G_n$ as well as $\langle n \rangle$ for some selected values of \sqrt{s} for both values $\sigma = 0.43$ fm and $\sigma = 0.53$ fm of the width parameter are shown in Figure 6.8. The observations made from Figure 6.7 are also valid for this figure. One should also note that changing the width parameter changes the expected value $\langle n \rangle$ very dramatically.

We still have one more experimentally obtainable quantity we can validate the eikonal minijet model against, the slope parameter B of $\frac{d\sigma_{\text{el}}}{dt} \propto e^{-B|t|}$. Approximating Equation (3.40) to the first order in the Mandelstam variable t yields

$$\begin{aligned} \frac{d\sigma_{\text{el}}}{dt} &\approx \pi \left(\int_0^{\infty} \Gamma(\mathbf{b}) \left(1 - \frac{b^2|t|}{4} \right) b db \right)^2 \\ &\approx \frac{d\sigma_{\text{el}}}{dt} \Big|_{t=0} \left(1 - |t| \left[\frac{1}{2} \frac{\int_0^{\infty} \Gamma(\mathbf{b}) b^3 db}{\int_0^{\infty} \Gamma(\mathbf{b}) b db} \right] \right) \\ &\approx \frac{d\sigma_{\text{el}}}{dt} \Big|_{t=0} e^{-B|t|}, \end{aligned} \tag{6.4}$$

where we have defined the slope parameter

$$B \equiv \frac{1}{2} \frac{\int_0^{\infty} \Gamma(\mathbf{b}) b^3 db}{\int_0^{\infty} \Gamma(\mathbf{b}) b db}. \tag{6.5}$$

We calculated B in the eikonal minijet model at various CMS energies \sqrt{s} with the width parameters $\sigma = 0.43$ fm and $\sigma = 0.53$ fm. These results are shown in Figure 6.9, along with experimental data from Refs. [43, 44, 45, 46, 47, 48, 49, 50]. The results calculated with the larger width parameter $\sigma = 0.53$ fm fit the experimental data, in fact, surprisingly well in the studied range, although the slope of B in \sqrt{s} seems to be slightly steeper in the experimental data than in the calculated results. Interestingly, this slope of B seems to be approximately same with $\sigma = 0.43$ fm and $\sigma = 0.53$ fm. The message of Figure 6.9 is rather obvious: the width parameter σ should apparently slightly still grow as a function of \sqrt{s} . Such fitting is, however, beyond the scope of this Master’s thesis.

Finally, we proceeded to calculate the probabilities G_n with $\sigma = 0.43$ fm taking also momentum conservation into account (Equation (5.5)) with Monte Carlo integration as described in Section 5.4. Because of the limited calculational capacity,

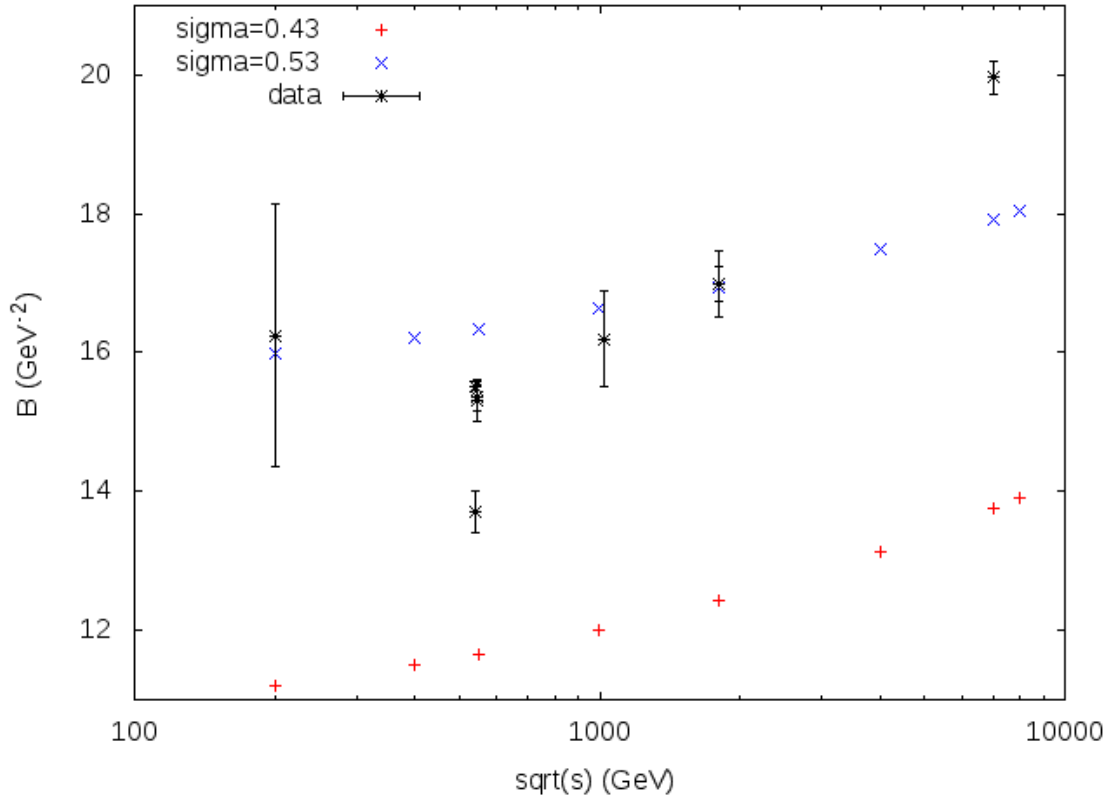


Figure 6.9: The slope parameter B as a function of the CMS energy \sqrt{s} , calculated from the eikonal minijet model with width parameter $\sigma = 0.43$ fm (red plus signs) and $\sigma = 0.53$ fm (blue crosses). The experimental data (black stars) is from [43, 44, 45, 46, 47, 48, 49, 50].

we only calculated the effect in the region $\sqrt{s} = 100 \dots 1000$ GeV and up to 8-fold minijet production, i.e. 24-dimensional integrals. In this region, we found the effect negligible, changing values of G_n by at most 3%. This result is not surprising, as from Figure 6.7 one can read that single dijet production dominates the σ_{in} in this region.

Chapter 7

Conclusion

In this thesis, we have derived the eikonal approximation for a quantum scattering problem. In this framework, we then studied an analytically simplistic model, the eikonal minijet model, for describing the CMS-energy dependence of the cross-sections in high energy proton–proton collisions. We then tested this model against experimental data gathered so far. As a part of our numerical analysis, we also studied the validity of the single effective subprocess approximation for minijet production at high energies. We found the approximation to be highly accurate at the energy scales studied.

The eikonal minijet model depends, in the leading order QCD perturbation theory, on two parameters, the momentum cutoff k_0 and the Gaussian thickness parameter σ . The cutoff k_0 sets the perturbatively calculable hard subprocesses apart from the nonperturbative soft subprocesses which we left untouched in this thesis as we lowered k_0 to as small values as possible. Using numerical analysis and varying the thickness σ from 0.43 fm to 0.53 fm, we found k_0 's so that our calculated total cross-sections for proton–proton collisions fit the experimental data in the CMS energy range $\sqrt{s} = 0.1 \dots 100$ TeV. Interestingly, $k_0 \gg \Lambda_{\text{QCD}}$ in all cases studied. With the model parameters fixed, we then proceeded to calculate predictions for inelastic scattering cross-sections in the mentioned range. Results of these calculations are shown in Figures 6.5 and 6.6. We found that despite its apparent simplicity, the model fit the experimental data surprisingly well.

The eikonal minijet model is based on the notion that inelastic proton–proton scattering on high energies can be treated perturbatively – in the collision one or more distinct pairs of partons, minijets, scatter from each other. Based on this we calculated within the framework of the model the probabilities of inelastic events to be understood as productions of n pairs of minijets. These probabilities are shown in Figure 6.7. As expected, the greater the energy of the colliding protons,

the more probable it is to have a multiple minijet production. In doing this, we updated and confirmed the results of Ref. [25].

As another test of the eikonal minijet model, we calculated the slope parameter B of the elastic differential cross section in the CMS energy range $\sqrt{s} = 0.1 \dots 10$ TeV, and compared it to experimental data. These results are shown in Figure 6.9. Even in this test, the eikonal minijet model represented experimental data surprisingly well, in spite of its simplicity.

A noteworthy detail of the model is that one does not need to impose strong ad hoc \sqrt{s} -scaling in the partonic overlap function A , even though protons appear to effectively widen at larger CMS energies. This effect is instead inherently taken care of via the fitting of the parameter k_0 and σ_{jet} which follows from k_0 . According to our results in Figure 6.6, once a fitting width parameter σ is found at some CMS energy, the same σ works well at all the CMS energies studied. Even so, as can be seen from Figure 6.9, the eikonal minijet model could perhaps represent the experimental data even better if some \sqrt{s} -dependence would be introduced in the overlap function A , which leads one also to reconsider the factorization of σ_{jet} from $A(b)$ assumed in Equation (4.5).

As the centre of momentum energy rises, the contribution of the multiple minijet production events in inelastic scattering cross-section increases. This raises a question of how does the conservation of momenta fit into the picture. The sum of the momenta of the partons participating in jet productions cannot be more than the initial momenta of the protons in the collision. To see if this plays a role in the probabilities of having multiple minijet production, one has to perform high-dimensional Monte Carlo integration. We calculated the effect of the momentum conservation on the probabilities of having multiple minijet productions in the region $\sqrt{s} = 100 \dots 1000$ GeV, up to 8-fold jet production, and found it negligible. This was somewhat expected, as in this region the production of one pair of minijets is very dominant. Studying the effect on higher energies was out of the scope of our work, as much more calculational capacity would be needed to perform the increasingly high-dimensional Monte Carlo Integrals.

Bibliography

- [1] M. Kuha. "Ultrarelativististen hadroni-hadroni -törmäysten kaksijettituoton aliprosessien vaikutusalojen laskeminen FeynCalcilla", Research training report, University of Jyväskylä, 2016.
- [2] K. J. Eskola. Lecture notes on course FYSH556 perturbative QCD, spring 2016.
- [3] R. P. Feynman. Very high-energy collisions of hadrons. *Phys. Rev. Lett.*, 23:1415–1417, 1969.
- [4] J. D. Bjorken and E. A. Paschos. Inelastic electron-proton and gamma-proton scattering and the structure of the nucleon. *Phys. Rev.*, 185:1975–1982, 1969.
- [5] M. E. Peskin and D. V. Schröder. *An Introduction To Quantum Field Theory*. Addison-Wesley Publishing Company, Boston, Massachusetts, 1995.
- [6] K. J. Eskola. Lecture notes on course FYSH300 particle physics, autumn 2015.
- [7] G. Sterman. *An Introduction to Quantum Field Theory*. Cambridge University Press, Cambridge, UK, 1993.
- [8] L. N. Lipatov. The parton model and perturbation theory. *Sov. J. Nucl. Phys.*, 20:94, 1975.
- [9] V. N. Gribov and L. N. Lipatov. Deep inelastic e p scattering in perturbation theory. *Sov. J. Nucl. Phys.*, 15:438, 1972.
- [10] G. Altarelli and G. Parisi. Asymptotic freedom in parton language. *Nucl. Phys.*, B126:298, 1977.
- [11] Y. L. Dokshitzer. Calculation of the structure functions for deep inelastic scattering and $e^+ e^-$ annihilation by perturbation theory in quantum chromodynamics. *Sov. Phys. JETP*, 46:641, 1977.

- [12] R. Paatelainen. Quark and gluon scatterings in the leading and next-to-leading order QCD perturbation theory. Master's thesis, University of Jyväskylä, 2010.
- [13] E. Eichten et al. Supercollider physics. *Rev. Mod. Phys.*, 56:579–707, 1984.
- [14] R. Cutler and D. Sivers. Quantum-chromodynamic gluon contributions to large-pt reactions. *Phys. Rev. D*, 17:196–211, 1978.
- [15] V. Shtabovenko, R. Mertig, and F. Orellana. New developments in FeynCalc 9.0. *Comput. Phys. Commun.*, 207:432–444, 2016. TUM-EFT 71/15, arXiv:1601.01167.
- [16] R. Mertig, M. Böhm, and A. Denner. FeynCalc - computer-algebraic calculation of Feynman amplitudes. *Comput. Phys. Commun.*, 64:345–359, 1991.
- [17] T. Hahn. Generating Feynman diagrams and amplitudes with FeynArts 3. *Comput. Phys. Commun.*, 140:418–431, 2001. arXiv:hep-ph/0012260.
- [18] M. Kuha. GitHub repository for research training, Open access at <http://github.com/mikromavitsus/erikoistyo>, cited 26.02.2017.
- [19] K. Kajantie, K. J. Eskola, and J. Lindfors. Quark and gluon production in high energy nucleus-nucleus collisions. *Nucl. Phys. B*, 323:37–52, 1989.
- [20] B. L. Combridge and C. J. Maxwell. Untangling large- p_T hadronic reactions. *Nucl. Phys. B239*, pages 429–458, 1984.
- [21] R. K. Ellis, W. J. Stirling, and B. R. Webber. *QCD and Collider Physics*. Cambridge University Press, Cambridge, UK, 1997.
- [22] V. Barone and E. Predazzi. *High-Energy Particle Diffraction*. Springer-Verlag Berlin Heidelberg, 2002. DOI:10.1007/978-3-662-04724-8.
- [23] U. Amaldi, M. Jacob, and G. Matthiae. Diffraction of hadronic waves. *Annu. Rev. Nucl. Sci.*, 26:385–456, 1976.
- [24] D. J. Griffiths. *Introduction to Quantum Mechanics*. Pearson Prentice Hall, 2005. ISBN:978-81-7758-230-7.
- [25] X. N. Wang. Role of multiple minijets in high-energy hadronic reactions. *Phys. Rev. D*, 43:104–112, 1991.
- [26] L. Durand and H. Pi. QCD and rising cross sections. *Phys. Rev. Lett.*, 58:303–306, 1987.

- [27] H. Niemi, K. J. Eskola, and R. Paatelainen. Event-by-event fluctuations in perturbative QCD + saturation + hydro model: pinning down QCD matter shear viscosity in ultrarelativistic heavy-ion collisions. *Phys. Rev. C*, 93:024907, 2016. arXiv:1505.02677 [hep-ph].
- [28] S. Chekanov et al. (ZEUS Collaboration). Exclusive electroproduction of J/ψ mesons at hermes. *Nucl. Phys. B*, 695:3–37, 2004. <http://arxiv.org/abs/hep-ex/0404008v1>.
- [29] M. Abramowitz and I. Stegun. *Handbook of Mathematical Functions with Formulas, Graphs, and Mathematical Tables*. Dover, New York, 1964.
- [30] G. Antchev et al. (TOTEM Collaboration). Luminosity-independent measurement of the proton–proton total cross section at $\sqrt{s}=8$ TeV. *Phys. Rev. Lett.*, 111:012001, 2013. DOI: 10.1103/PhysRevLett.111.012001.
- [31] S. Chatrchyan et al. (CMS Collaboration). Measurement of the inelastic proton–proton cross section at $\sqrt{s} = 7$ tev. *Phys. Lett. B*, 722:5–27, 2013.
- [32] B. Abelev et al. (ALICE Collaboration). Measurement of inelastic, single- and double-diffraction cross sections in proton–proton collisions at the LHC with ALICE. *Eur. Phys. J.*, C73:2456, 2013. arXiv:1208.4968v2 [hep-ex].
- [33] G. Aad et al. (ATLAS Collaboration). Measurement of the inelastic proton–proton cross-section at $\sqrt{s} = 7$ TeV with the ATLAS detector. *Nat. Commun.*, 2:463, 2011. DOI: 10.1038/ncomms1472.
- [34] G. Antchev et al. (TOTEM Collaboration). Luminosity-independent measurements of total, elastic and inelastic cross-sections at $\sqrt{s} = 7$ TeV. *Europhys. Lett.*, 101:21004, 2013. DOI: 10.1209/0295-5075/101/21004.
- [35] K.A. Olive et al. (Particle Data Group). Data files and plots of cross-sections and related quantities in the 2014 review of particle physics. *Chin. Phys. C*, 38:090001, 2014. URL: <http://pdg.lbl.gov/2016/hadronic-xsections/>.
- [36] M. Kuha. GitHub repository for numerical analyses in master’s thesis, Open access at <http://github.com/mikromavitsus/Gradu>, cited 26.02.2017.
- [37] A. Buckley et al. LHAPDF6: parton density access in the LHC precision era. *Eur. Phys. J.*, C75:132, 2015. arXiv:1412.7420 [hep-ph].
- [38] S. Dulat, T. J. Hou, J. Gao, M. Guzzi, J. Huston, P. Nadolsky, J. Pumplin, C. Schmidt, D. Stump, and C. P. Yuan. New parton distribution functions from a global analysis of quantum chromodynamics. *Phys. Rev. D*, 93:033006, 2016. arXiv:1506.07443 [hep-ph].

- [39] S. G. Johnson. Open access C library, homepage <http://ab-initio.mit.edu/wiki/index.php/Cubature>, cited 26.02.2017.
- [40] M. Galassi et al. Gnu scientific library reference manual (3rd ed.). Open access C library, homepage <http://www.gnu.org/software/gsl/>, cited 26.02.2017.
- [41] J. R. Cudell et al. (COMPETE Collaboration). Benchmarks for the forward observables at rhic, the tevatron-run ii, and the lhc. *Phys. Rev. Lett.*, 89:201801, 2002. DOI: 10.1103/PhysRevLett.89.201801.
- [42] K.J. Eskola, K. Kajantie, P.V. Ruuskanen, and K. Tuominen. Scaling of transverse energies and multiplicities with atomic number and energy in ultrarelativistic nuclear collisions. *Nucl. Phys. B*, 570:379–389, 2000. arXiv: hep-ph/9909456.
- [43] G. Antchev et al. (TOTEM Collaboration). Measurement of proton-proton elastic scattering and total cross-section at $\sqrt{s} = 7$ TeV. *Europhys. Lett.*, 101:21002, 2013. DOI: 10.1209/0295-5075/101/21002.
- [44] M. Bozzo et al. (UA4 Collaboration). Low momentum transfer elastic scattering at the CERN proton–anti-proton collider. *Phys. Lett.*, 147B:385–391, 1984. DOI:10.1016/0370-2693(84)90138-2.
- [45] R. Battiston et al. (UA4 Collaboration). Proton–anti-proton elastic scattering at four momentum transfer up to $0.5 - \text{GeV}^2$ at the CERN SPS collider. *Phys. Lett.*, 127B:472–475, 1983. DOI:10.1016/0370-2693(83)90296-4.
- [46] C. Augier et al. (UA4/2 Collaboration). A precise measurement of the real part of the elastic scattering amplitude at the s anti-p p s. *Phys. Lett.*, B316:448–454, 1993. DOI:10.1016/0370-2693(93)90350-Q.
- [47] S. Bueltmann et al. (pp2pp Collaboration). First measurement of proton-proton elastic scattering at RHIC. *Phys. Lett.*, B579:245–250, 2004. DOI:10.1016/j.physletb.2003.11.023.
- [48] F. Abe et al. (CDF Collaboration). Measurement of small angle $\bar{p}p$ elastic scattering at $\sqrt{s} = 546$ GeV and 1800 GeV. *Phys. Rev.*, B50:5518–5534, 1994. DOI:10.1103/PhysRevD.50.5518.
- [49] N. A. Amos et al. (E710 Collaboration). Measurement of ρ , the ratio of the real to imaginary part of the $\bar{p}p$ forward elastic scattering amplitude, at $\sqrt{s} = 1.8 - \text{TeV}$. *Phys. Rev. Lett.*, 68:2433–2436, 1992. DOI:10.1103/PhysRevLett.68.2433.

- [50] N. A. Amos et al. (E710 Collaboration). $\bar{p}p$ elastic scattering at $\sqrt{s} = 1020 - \text{GeV}$. *Nuovo Cim.*, A106:123–132, 1993. DOI:10.1007/BF02771512.
- [51] G. Leibbrandt. Introduction to noncovariant gauges. *Rev. Mod. Phys.*, 59:1067–1115, 1977.
- [52] L. D. Faddeev and V.N. Popov. Feynman diagrams for the Yang-Mills field. *Phys. Lett.*, B25:29, 1967.
- [53] P. Paakkinen. Dokshitzer–Gribov–Lipatov–Altarelli–Parisi evolution equations. Master’s thesis, University of Jyväskylä, 2015.
- [54] R. Paatelainen. Minijet initial state of heavy-ion collisions from next-to-leading order perturbative QCD. Doctoral dissertation, University of Jyväskylä, 2014.

Appendix A

Quantum Chromodynamics tools

In this Chapter we show and derive some technical tools for our calculations. The discussion is inspired by [2].

A.1 Gluon propagators

Quantum Chromodynamics is a non-Abelian gauge theory with a local SU(3) gauge symmetry. The Lagrangian is written as [2] [5, 15.2]

$$\mathcal{L} = -\frac{1}{4} \sum_{\mu,\nu=0}^3 \sum_{a=1}^8 F^{\mu\nu,a} F_{\mu\nu,a} + \sum_q \left[i \sum_{i,j=1}^3 (\bar{\psi}_q)_i \not{D}_{ij} (\psi_q)_j - m_q \bar{\psi}_q \psi_q \right], \quad (\text{A.1})$$

where the SU(3) Maxwell's field tensor is

$$F_{\mu\nu}^a = \partial_\mu A_\nu^a - \partial_\nu A_\mu^a - g_s \sum_{b,c=1}^8 f^{abc} A_\mu^b A_\nu^c, \quad (\text{A.2})$$

field $A^{\mu,a}$ is the gluon field with colour a , g_s is the strong coupling constant, f^{abc} are the structure constants of SU(3), $(\psi_q)_j$ is a spinor with colour j corresponding to a quark flavour $q = u, d, c, s, t, b$, and m_q is the mass of the quark q . The covariant derivative \not{D}_{ij} is

$$\not{D}_{ij} = \sum_{\mu=0}^3 \gamma_\mu D_{ij}^\mu = \sum_{\mu=0}^3 \gamma_\mu \left(\partial^\mu (\mathbb{I}_3)_{ij} + i g_s \sum_{a=1}^8 A^{\mu,a} (t^a)_{ij} \right), \quad (\text{A.3})$$

where t^a are the generators of SU(3).

For unique solutions involving the gauge field A^μ , we have to fix a gauge condition.

For exhaustive discussion on different gauges, see Ref. [51]. One such condition is

$$\sum_{\mu=0}^3 \partial_{\mu} A^{\mu} = 0, \quad (\text{A.4})$$

which is called Lorenz gauge condition. It is implemented in the Lagrangian via the Lagrange multiplier λ :

$$\mathcal{L}' = \mathcal{L} - \frac{1}{2\lambda} \sum_{a=1}^8 \left(\sum_{\mu=0}^3 \partial_{\mu} A^{\mu,a} \right) \left(\sum_{\mu=0}^3 \partial_{\mu} A^{\mu,a} \right). \quad (\text{A.5})$$

This gauge condition leads to following Feynman rule for gluon propagators [2, 5]:

$$\mu, a \begin{array}{c} \text{oooooo} \\ \xrightarrow{k} \end{array} \nu, b = -\frac{i\delta^{ab}}{k^2} \left(g^{\mu\nu} - (1-\lambda) \frac{k^{\mu} k^{\nu}}{k^2} \right).$$

Leaving λ arbitrary is often referred to as general covariant gauge, whereas the choice $\lambda = 0$ is called Landau gauge and $\lambda = 1$ Feynman gauge.

Another choice could be an axial gauge, where the gauge field A^{μ} satisfies

$$\sum_{\mu=0}^3 n_{\mu} A^{\mu} = 0, \quad (\text{A.6})$$

for some arbitrary four-vector n . Similar to the Lorenz condition (A.4), this condition can be implemented into Lagrangian via

$$\mathcal{L}' = \mathcal{L} - \frac{1}{2\lambda} \sum_{a=1}^8 \left(\sum_{\mu=0}^3 n_{\mu} A^{\mu,a} \right) \left(\sum_{\mu=0}^3 n_{\mu} A^{\mu,a} \right). \quad (\text{A.7})$$

This gauge choice leads to following Feynman rule for gluon propagators:

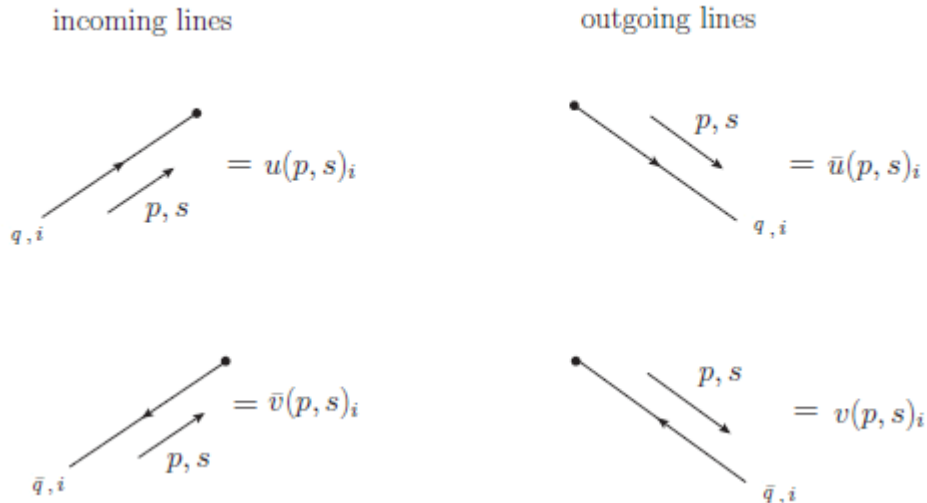
$$\mu, a \begin{array}{c} \text{oooooo} \\ \xrightarrow{k} \end{array} \nu, b = -\frac{i\delta^{ab}}{k^2} \left(g^{\mu\nu} - \frac{n^{\mu} k^{\nu} + k^{\mu} n^{\nu}}{n \cdot k} + n^2 (1 - \lambda \frac{k^2}{n^2}) \frac{k^{\mu} k^{\nu}}{(n \cdot k)^2} \right).$$

As the general axial gauge makes many calculations very complicated due to the rapidly increasing number of terms, one often makes further assumptions on the vector n . One popular restriction is $n^2 = \lambda = 0$, dubbed light-cone gauge. Note also that if in a given Feynman graph there are more than one gluons, they must each fulfil their gauge conditions separately. By making this observation, one can choose a different n for each external leg, for example, to make calculations more practical. Although they are noticeably more intricate than Lorenz gauges,

axial gauges have one clear superiority. In them, by construction, only transverse polarisations propagate. Thus no Faddeev-Popov ghosts [52] emerge. For this reason, axial gauges are sometimes called physical gauges.[51, 53]

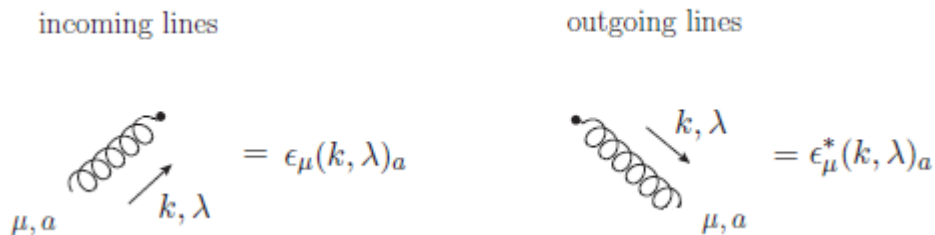
In this thesis the following convention for QCD Feynman rules [2, 5, 54] is used:

External lines of quarks or antiquarks with momentum p , spin s , and colour index $i = 1, 2, 3$:



where u and v are the quark spinors.

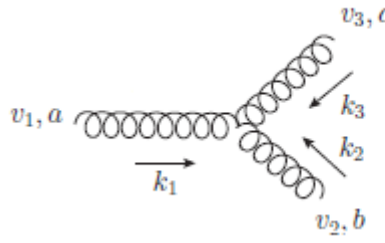
External lines of gluons of momentum k , polarization λ and colour index $a = 1, \dots, 8$:



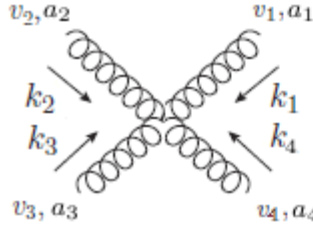
where ϵ is the polarization vector.

Quark–gluon coupling, three-gluon coupling, and four-gluon coupling vertices:





$$= -gf^{abc} \left[g^{v_1 v_2} (k_1 - k_2)^{v_3} + g^{v_2 v_3} (k_2 - k_3)^{v_1} + g^{v_3 v_1} (k_3 - k_1)^{v_2} \right]$$



$$= -ig^2 \left[f^{ea_1 a_2} f^{ea_3 a_4} (g_{\nu_1 \nu_3} g_{\nu_2 \nu_4} - g_{\nu_1 \nu_4} g_{\nu_2 \nu_3}) + f^{ea_1 a_3} f^{ea_2 a_4} (g_{\nu_1 \nu_4} g_{\nu_3 \nu_2} - g_{\nu_1 \nu_2} g_{\nu_3 \nu_4}) + f^{ea_1 a_4} f^{ea_2 a_3} (g_{\nu_1 \nu_2} g_{\nu_4 \nu_3} - g_{\nu_1 \nu_3} g_{\nu_4 \nu_2}) \right]$$

where g is the strong coupling constant, T^a are the SU(3) generator matrices in fundamental representation, γ^μ are the Dirac γ matrices, and f^{abc} are the SU(3) structure constants.

A.2 Polarisation tensor in Lorenz gauge

Leaving all summations and colour indices implicit, in the Lorenz gauge the QCD gluon Lagrangian reads

$$\mathcal{L} = -\frac{1}{4}F^{\mu\nu}F_{\mu\nu} - \frac{1}{2\lambda}(\partial_\mu A^\mu)^2. \quad (\text{A.8})$$

Euler-Lagrange Equation for the gluon field then gets the form

$$\square A^\nu - (1 - \lambda)\partial^\nu(\partial_\mu A^\mu) = 0. \quad (\text{A.9})$$

Contracting then with ∂_ν yields us

$$\lambda\square(\partial_\mu A^\mu) = 0, \quad (\text{A.10})$$

which implies

$$\partial^\nu(\partial_\mu A^\mu) = C^\nu, \quad (\text{A.11})$$

where C^ν are constants in x^ν . Substituting this result into (A.9) gives

$$\square A^\nu = (1 - \lambda)C^\nu. \quad (\text{A.12})$$

As this must hold for any λ , the only possibility is that $C^\nu = 0$. The gauge field A^ν must therefore satisfy the wave equation

$$\square A^\nu = 0. \quad (\text{A.13})$$

The wave Equation is solved by plane waves

$$A^\nu = \epsilon^\nu(k)e^{-ik \cdot x}. \quad (\text{A.14})$$

On the other hand, the Euler-Lagrange Equation (A.9) now leaves just

$$(1 - \lambda)\partial^\nu(\partial_\mu A^\mu) = 0 \quad \forall \lambda, \quad (\text{A.15})$$

which implies that

$$\partial_\mu A^\mu = D, \quad (\text{A.16})$$

where D is a scalar constant in x . Now differentiating Equation (A.14) leads to

$$\partial_\mu A^\mu = (\partial_\mu \epsilon^\mu(k))e^{-ik \cdot x} - ik \cdot \epsilon(k)e^{-ik \cdot x} = -ik \cdot \epsilon(k)e^{-ik \cdot x} = D. \quad (\text{A.17})$$

For D and $\epsilon(k)$ to be independent of x , this then implies that

$$D = k \cdot \epsilon(k) = 0. \quad (\text{A.18})$$

Thus, $\partial_\mu A^\mu = 0$ and $k_\mu A^\mu = 0$.

Gluon field A^μ transforms under gauge transformations as

$$\tilde{A}^\mu = A^\mu - \partial^\mu \beta(x), \quad (\text{A.19})$$

where $\beta(x)$ is some arbitrary function of x . For the Lorenz condition $\partial_\mu A^\mu = 0$ to hold, the function $\beta(x)$ must satisfy

$$\square \beta(x) = 0 \quad \Leftrightarrow \quad \beta(x) = B(k) e^{-ik \cdot x}. \quad (\text{A.20})$$

Remembering condition (A.18) and that $k^2 = 0$, we can write the polarization vector $\epsilon^\mu(k)$ as

$$\epsilon^\mu(k) = \alpha(k) k^\mu + \epsilon'^\mu(k), \quad (\text{A.21})$$

where $\alpha(k)$ is some real number and $k \cdot \epsilon'(k) = 0$. Combining Equations A.19, A.20, and A.21 yields

$$\tilde{A}^\mu = [(\alpha(k) + iB(k))k^\mu + \epsilon'^\mu(k)] e^{-ik \cdot x}. \quad (\text{A.22})$$

This can be interpreted as such that we always have some freedom in choosing the polarization vector, as we can then afterwards do a gauge transform such that the term $(\alpha(k) + iB(k))$ vanishes for one component of $\epsilon^\mu(k)$. Therefore let us choose the polarization vector $\epsilon^\mu(k)$ so that

$$\epsilon^0 = 0, \quad \text{from which } \mathbf{k} \cdot \epsilon = 0, \quad (\text{A.23})$$

follows from the Equation (A.18).

Define now $\tilde{k} = (k^0, -\mathbf{k})$, a linearly independent vector of the vector $k = (k^0, \mathbf{k})$. Now (A.23) implies that

$$\tilde{k} \cdot \epsilon(k) = 0. \quad (\text{A.24})$$

Let us then define a polarisation tensor \mathcal{P} by

$$\mathcal{P}^{\mu\nu} = \sum_{\lambda} \epsilon_{\lambda}^{\mu}(k) \epsilon_{\lambda}^{*\nu}(k), \quad (\text{A.25})$$

where the summation is taken over the physical polarisation states $\lambda = 1, 2$. Let

the polarisation vectors ϵ be normalized to unity, i.e.

$$\epsilon_\lambda(k) \cdot \epsilon_\lambda^*(k) = -1. \quad (\text{A.26})$$

Now using the definition (A.25) and constraints (A.18), (A.24), and (A.26), we get the following identities for the polarisation tensor:

$$g_{\mu\nu}\mathcal{P}^{\mu\nu} = -2, \quad k_\mu\mathcal{P}^{\mu\nu} = k_\mu k_\nu\mathcal{P}^{\mu\nu} = 0, \quad \tilde{k}_\mu\mathcal{P}^{\mu\nu} = \tilde{k}_\mu\tilde{k}_\nu\mathcal{P}^{\mu\nu} = 0. \quad (\text{A.27})$$

The polarisation tensor is a second rank tensor, so it is uniquely fixed by two linearly independent vectors \tilde{k} and k , and the metric g . Using this we can decompose it as

$$\mathcal{P}^{\mu\nu} = Ag^{\mu\nu} + Bk^\mu k^\nu + C\tilde{k}^\mu\tilde{k}^\nu + D\tilde{k}^\mu k^\nu + Ek^\mu\tilde{k}^\nu, \quad (\text{A.28})$$

where A, B, C, D , and E are some scalars. The scalars can be determined by imposing the constraints (A.27). This yields us the form

$$\mathcal{P}^{\mu\nu} = -g^{\mu\nu} + \frac{1}{\tilde{k} \cdot k} \left(\tilde{k}^\mu k^\nu + k^\mu \tilde{k}^\nu \right). \quad (\text{A.29})$$

A.3 Polarisation tensor in axial gauge

Again leaving all summations and colour indices implicit, in an axial gauge the QCD Lagrangian for gluons reads

$$\mathcal{L} = -\frac{1}{4}F^{\mu\nu}F_{\mu\nu} - \frac{1}{2\lambda}(n_\mu A^\mu)^2. \quad (\text{A.30})$$

Euler-Lagrange Equation for the gluon field then gets the form

$$-\lambda(n \cdot A)n^\nu + \square A^\nu - \partial^\nu(\partial_\mu A^\mu) = 0. \quad (\text{A.31})$$

Contraction with one-form n_ν then yields a differential equation

$$-\lambda n^2(n \cdot A) + \square(n \cdot A) - (n \cdot \partial)(\partial_\mu A^\mu) = 0. \quad (\text{A.32})$$

Fourier transforming this yields us the equivalent algebraic Equation in momentum space

$$-\lambda n^2(n_\mu \tilde{A}^\mu) + k^2(n_\mu \tilde{A}^\mu) - (n \cdot k)(\partial_\mu \tilde{A}^\mu) = 0 \quad (\text{A.33})$$

$$\Leftrightarrow [(\lambda n^2 - k^2)n_\mu + (n \cdot k)k_\mu] \tilde{A}^\mu = 0. \quad (\text{A.34})$$

Now as neither factor $(\lambda n^2 - k^2)$ nor $(n \cdot k)$ vanishes generally, and vectors n and k are linearly independent, for Equation (A.33) to hold also

$$n \cdot \tilde{A} = k \cdot \tilde{A} = 0 \quad (\text{A.35})$$

must hold. Inverse Fourier transforming these yields straightforwardly

$$n \cdot A = k \cdot A = 0. \quad (\text{A.36})$$

Substituting (A.36) into (A.31) gives then

$$\square A^\nu = \partial^\nu(\partial_\mu A^\mu), \quad (\text{A.37})$$

which is solved by plane waves

$$A^\mu = \epsilon^\mu(k)e^{-ik \cdot x}, \quad (\text{A.38})$$

where the polarisation vector $\epsilon^\mu(k)$ must, due to (A.36), be chosen such that

$$k \cdot \epsilon(k) = 0. \quad (\text{A.39})$$

This can be done because of how A^μ transforms under gauge transformations (see Section A.2). Now the constraint (A.36) gives also

$$n \cdot A = (n \cdot \epsilon(k)) e^{-ik \cdot x} = 0 \quad \Leftrightarrow \quad n \cdot \epsilon(k) = 0. \quad (\text{A.40})$$

Let us, similar to what we did in the Lorenz gauge, then define polarisation tensor \mathcal{P} by

$$\mathcal{P}^{\mu\nu} = \sum_{\lambda} \epsilon_{\lambda}^{\mu}(k) \epsilon_{\lambda}^{*\nu}(k), \quad (\text{A.41})$$

where the summation is taken over the physical polarisation states $\lambda = 1, 2$. Let the polarisation vectors ϵ be normalized to unity, i.e.

$$\epsilon_{\lambda}(k) \cdot \epsilon_{\lambda}^*(k) = -1. \quad (\text{A.42})$$

Now using the definition (A.41) and constraints (A.39), (A.40), and (A.42), we get the following identities for the polarisation tensor:

$$g_{\mu\nu} \mathcal{P}^{\mu\nu} = -2, \quad k_{\mu} \mathcal{P}^{\mu\nu} = k_{\mu} k_{\nu} \mathcal{P}^{\mu\nu} = 0, \quad n_{\mu} \mathcal{P}^{\mu\nu} = n_{\mu} n_{\nu} \mathcal{P}^{\mu\nu} = 0. \quad (\text{A.43})$$

Again, as in Equation (A.28), we can decompose the polarization tensor as

$$\mathcal{P}^{\mu\nu} = A g^{\mu\nu} + B k^{\mu} k^{\nu} + C n^{\mu} n^{\nu} + D n^{\mu} k^{\nu} + E k^{\mu} n^{\nu}, \quad (\text{A.44})$$

where A, B, C, D , and E are some scalars. The scalars can be determined by imposing the constraints (A.43). This yields us the form

$$\mathcal{P}^{\mu\nu} = -g^{\mu\nu} + \frac{1}{n \cdot k} (n^{\mu} k^{\nu} + k^{\mu} n^{\nu}) - \frac{n^2}{(n \cdot k)^2} k^{\mu} k^{\nu}. \quad (\text{A.45})$$

Appendix B

Integrating in momentum fraction space

One could be interested in changing the integrals in Equations (2.13) and (2.26) into the momentum fraction space (k_T^2, x_1, x_2) . For completeness, this approach is discussed below. Inverting the Equations (2.7) and (2.8) yields

$$y_1 = \log \left[\frac{\sqrt{s}}{2x_2 k_T} \left(x_1 x_2 - \sqrt{x_1 x_2 \left(x_1 x_2 - \frac{4k_T^2}{s} \right)} \right) \right], \quad (\text{B.1})$$

$$y_2 = \log \left[\frac{\sqrt{s}}{2x_2 k_T} \left(x_1 x_2 + \sqrt{x_1 x_2 \left(x_1 x_2 - \frac{4k_T^2}{s} \right)} \right) \right]. \quad (\text{B.2})$$

Using these results the integration measures in Equations (2.13) and (2.26) can be written with

$$dy_1 dy_2 = \left| \frac{\partial(y_1, y_2)}{\partial(x_1, x_2)} \right| dx_1 dx_2 = \frac{dx_1 dx_2}{\sqrt{x_1 x_2 \left(x_1 x_2 - \frac{4k_T^2}{s} \right)}}, \quad (\text{B.3})$$

in (k_T^2, x_1, x_2) space, where the integration limits are much simpler:

$$k_0^2 \leq k_T^2 \leq \frac{s}{4}, \quad (\text{B.4})$$

$$\frac{4k_T^2}{s} \leq x_1 \leq 1, \quad (\text{B.5})$$

$$\frac{4k_T^2}{s x_1} \leq x_2 \leq 1. \quad (\text{B.6})$$

Some further thinking still needs to be done in changing the basis. The coordinate transformations (2.7) and (2.8) are not injective; they are symmetric under the

exchange of y_1 and y_2 . There is no such symmetry in (B.1) and (B.2), $y_{1,2}(x_1, x_2) \neq y_{1,2}(x_2, x_1)$, but we could have chosen to write these equations the other way around with (B.1) for y_2 and (B.2) for y_1 . Taking these considerations into account, to calculate the integral in the whole phase space, the transformation of the integral would need to be

$$\int F(y_1, y_2) dy_1 dy_2 = \int \left(F(y_1(x_1, x_2), y_2(x_1, x_2)) + F(y_2(x_1, x_2), y_1(x_1, x_2)) \right) \left| \frac{\partial(y_1, y_2)}{\partial(x_1, x_2)} \right| dx_1 dx_2. \quad (\text{B.7})$$

This also demonstrates the usefulness of the rapidity basis in doing the phase space integrals.